Gamma-Ray Spectroscopy

18

William L. Dunn, Douglas S. McGregor, and J. Kenneth Shultis

Contents

W. L. Dunn · J. K. Shultis
Mechanical and Nuclear Engineering, Kansas State University, Manhattan, KS, USA
e-mail: dunn@mne.ksu.edu; jks@ksu.edu

D. S. McGregor (✉)
Semiconductor Materials and Radiological Technologies Laboratory, Mechanical and Nuclear Engineering, Kansas State University, Manhattan, KS, USA
e-mail: mcgregor@ksu.edu

I. Fleck et al. (eds.), *Handbook of Particle Detection and Imaging*,
https://doi.org/10.1007/978-3-319-93785-4_17

Abstract

The common methods of analyzing gamma-ray spectra obtained from detectors capable of energy discrimination are discussed. Gamma-ray spectra generally are in the form of detector response *versus* discrete channel number. The methods considered for gamma-ray spectroscopy are somewhat general and can be applied to other types of spectroscopy. The general objective of spectroscopy is to obtain, at a minimum, the qualitative identification of the source (e.g., source energies or radionuclides present). However, most spectroscopy applications seek quantitative information also, as expressed by, e.g., the source strength or the radionuclide concentration. Various methods for qualitative and quantitative analysis are summarized, and illustrative examples are provided. A review of detectors used for gamma-ray spectroscopy is included.

Nomenclature

Most of the symbols used in this chapter are briefly identified here. More complete descriptions of the symbols are provided within the text.

A	source activity
A_{es}	escape peak counts
A_j	net peak counts
A_p	peak counts
$b(h)$	background density function
b_n	background counts in channel n
$B(n)$	background in channel n
c	speed of light
$c(n)$	response rate function
$C(n)$	response cumulative function
C_h	heat capacity
d	spacing between crystal planes
Δ	channel width
E	photon energy
E_{bs}	backscatter photon energy
E'	apparent energy
E_d	energy deposited in detector
E_{es}	escape peak energy
E_j	jth discrete energy emitted by source

E_p	peak energy
ϵ_{es}	escape peak efficiency
ϵ_I	total intrinsic efficiency
ϵ_{peak}	peak efficiency
η_{rel}	HPGe relative efficiency
f	function that relates h to E_d
F	Fano factor S_j
FWHM	full width at half maximum
g	Gaussian density function
G	dynode gain
h	pulse height
h_0	centroid of pulse-height peak
ϵ	detector efficiency
j	subscript for discrete energy
j	subscript for discrete energy
J	number of discrete energies
k	subscript for nuclide
$\mathtt{k}$	Boltzmann's constant
K	number of nuclides
λ	photon wavelength
M	subset of N
m_e	electron rest mass
m	number of overlapping peaks
$\mu_{e,h}$	charge mobility (electrons, holes)
$\tilde{n}$	continuous channel number
n	discrete channel number
N	number of channels
$\tilde{n}$	continuous channel number
n	discrete channel number
N_o	initial number of charge pairs
ν	number of degrees of freedom
ξ_k	nuclide concentration
$\xi_{e,h}$	carrier extraction factor
PCR	peak-to-Compton ratio
PVR	peak-to-valley ratio
PTR	peak-to-total ratio
q	unit electronic charge
Q	total induced charge
Q_o	initial excited charge
$\mathcal{R}$	detector resolution
$R(h)$	cumulative counts with pulse height $< h$
$r(h)$	count rate with pulses about h
$\mathcal{R}_n(E)$	detector response function
$\mathcal{R}(h\|E)$	detector response kernel
$s(E)$	source density function

s_c	continuum emission rate
s_j	emission rate at energy
E_j	emission rate over time $\overline{T}$
σ	standard deviation
T_{cs}	Compton electron kinetic energy
T_{pe}	photoelectron kinetic energy
t	live time
$\overline{T}$	counting time
T	absolute temperature
$\tau_{e,h}$	charge carrier lifetime
u	detector response function
$v_{e,h}$	charge carrier velocity
w	average ionization energy
W_n	weight factor
W_d	detector width
χ_v^2	reduced chi-square function
y	response model
z	composite detector kernel
X_k	basis vector

Introduction

Gamma rays and x rays are photons of electromagnetic radiation that are capable of causing ionization. Technically, x rays differ from gamma rays in their source of origin, but for practical purposes, this is irrelevant, and photon spectra can be analyzed by the same methods whether the source photons are x rays or gamma rays. As a practical matter, photons of energy less than about 10 keV are difficult to detect because they are easily absorbed by the detector housing. The concepts that are discussed here can be applied, in principle, to spectra from photons of energy less than 10 keV and also to spectra generated by other particles, such as electrons. For instance, x-ray photoelectron spectroscopy (XPS) and electron scattering for chemical analysis (ESCA) lead to electron spectra that can be analyzed by the methods discussed here. Thus, it is understood that reference to "gamma-ray spectroscopy" is an oversimplification and many of the methods discussed here can be applied to spectra generated by x rays, gamma rays, or other types of radiation.

Gamma-ray spectroscopy is a general area of study within which spectra are analyzed in order to determine qualitative and, if possible, quantitative information about a sample under investigation. Spectra generally refer to collections of data for which the independent variable is channel number (or a related quantity such as pulse height, energy, or wavelength) and the dependent variable is a detector response that depends on the independent variable. Spectra are generated in various processes, such as energy-dispersive x ray fluorescence (EDXRF), neutron activation analysis (NAA), prompt gamma neutron activation analysis (PGNAA), XPS, and general counting of unknown radioactive sources. Often, spectroscopy

is directed at the quantitative objective of identifying concentrations of specific elements or isotopes (henceforth, the generic term "nuclides" is used) that are present in samples, but it also can be employed in a qualitative manner to identify whether specific gamma-ray-emitting nuclides, such as those in special nuclear materials, are present in samples.

In general, a sample that is under investigation emits photons whose energies are characteristic of the nuclides present in the sample. The photons may be excited by an external source or the sample may emit these photons spontaneously. A careful spectroscopic investigation generally seeks to determine either the energies emitted and their intensities or the nuclides present and their concentrations. In the remainder of this chapter, attention is given to photon spectra that are generated from samples interrogated by any of a number of means, active or passive, to determine information about the constituents of the sample. Much of the material presented here is extracted from McGregor and Shultis (2020).

Basic Concepts

Many photon detectors can produce responses that are proportional to the energy deposited in the detector. These include proportional counters, scintillation detectors, and semiconductor detectors. Regardless of the detector, a voltage pulse is created whose amplitude h, generally called the *pulse height*, is a function of the energy deposited E_d in the detector, i.e.,

$$h = f(E_d), \tag{1}$$

where f is some function. For many detectors, f is linear and

$$h = \alpha + \beta E_d, \tag{2}$$

where α and β are constants unique to a detector. However, scintillation detectors, in particular, can exhibit nonlinearities, especially at low photon energies, and this nonlinearity should be taken into account. Linearity of a detector is often expressed in terms of the pulse height per unit energy as a function of the deposition energy, a quantity which is constant for a linear detector. In any event, a good spectroscopist should know f, the functional relationship between pulse height and deposited energy, for any spectroscopic detector used.

In gamma spectroscopy, the pulse height h is measured, and the deposited energy E_d is obtained by inversion of Eq. (1), namely,

$$E_d = f^{-1}(h), \tag{3}$$

or if the spectrometer is linear, then

$$E_d = \frac{h - \alpha}{\beta}. \tag{4}$$

Moreover, the pulse heights produced by repeated deposition of energy E_d in a detector are not exactly the same; rather, they are distributed about a mean value $h_0 = f(E_d)$ by some kernel $g(h|E_d)$ such that $g(h|E_d)dh$ is the probability an event that deposits energy E_d in the detector results in a pulse with an amplitude in dh about h. In gamma-ray spectroscopy, this *spreading* kernel has a shape similar to a Gaussian shape although, in practice, it is usually skewed slightly toward lower amplitudes as a consequence of different collection times of charge carriers produced in different regions of the detector and the different amount of recombination and trapping they experience as they are collected. Shallow angle Compton scattering also contributes slightly to this asymmetry. An example of this amplitude kernel for an HPGe detector is shown in Fig. 1. In effect, the detector systems that produce the voltage pulses operate on the energy deposited E_d with an energy kernel $z(E_d, E')$ that transforms E_d into a range of "apparent" energies E', which are centered on E_d. The resolution of a spectrometer is determined by the degree to which pulse amplitudes are spread out around h_0 or around E_d and is quantified by the full width at half maximum (FWHM) either as a percent or in energy units.

Often the amplitude spreading kernel is approximated by the Gaussian probability distribution

$$g(h|h_0, \sigma) = \frac{1}{\sqrt{2\pi}\sigma} \exp[-(h - h_0)^2/(2\sigma^2)], \tag{5}$$

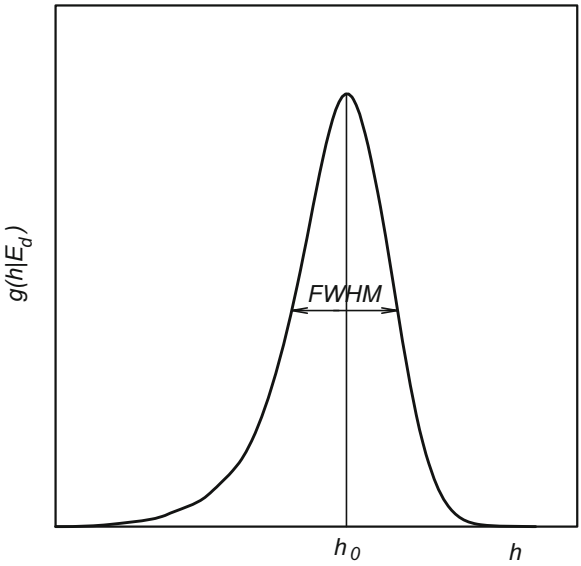

Fig. 1 A pulse-height spreading kernel for an HPGe detector as measured for the 1173-keV ^{60}Co gamma ray [IEEE-325 1996]. Note the peak is not quite symmetric about the centroid $h_{\max}$

where h_0 is the mean value or centroid and σ is the standard deviation. The peak value of the Gaussian PDF occurs at the centroid and is given by $g_{\max} = 1/(\sqrt{2\pi}\sigma)$. Note that for a Gaussian distribution FWHM $= 2\sqrt{2\ln 2}\sigma \simeq 2.355\sigma$.

It is worth noting that the energy resolution of semiconductor detectors is, in general, significantly better than that for scintillation detectors or proportional counters. McGregor (2016) gives a good comparative description of the resolution of various detector types. Each type of detector has its advantages and disadvantages. Several chapters in this book on the various detector types provide useful information on the characteristics of each type of detector.

The pulse heights are scaled to be within a finite interval $[h_{\min}, h_{\max}]$. Typically, these limits are $h_{\min} = 0$ and $h_{\max} = 10\,\mathrm{V}$. In any case, the variables E_d and h are continuous variables. Whatever the pulse-height limits are, the response of a detector is typically binned into discrete "channels." If n denotes an individual discrete (integral) channel number and N is the total number of channels, then the channel width is

$$\Delta = \frac{h_{\max} - h_{\min}}{N}.$$

The channel numbers are related to the detected magnitudes of the voltage pulses (pulse heights) by the relations

$$\begin{aligned} n &= 1, \text{ if } h_{\min} < h \le h_{\min} + \Delta \\ &= 2, \text{ if } h_{\min} + \Delta < h \le h_{\min} + 2\Delta \\ &\vdots \\ &= N, \text{ if } h_{\min} + (N-1)\Delta < h \le h_{\min} + N\Delta. \end{aligned} \tag{6}$$

Thus, the measured continuous pulse heights are converted into discrete channels, and each pulse registers a count in one and only one channel. NIM multichannel analyzer systems confine voltage signals or pulse heights to be within 0–10 volts. Hence, a binary system may be subdivided with 2^N voltage bins over the 10-volt range. For $N = 10$, there are 1024 bins, or *channels*, over the 10-volt range having, in this case, 9.8×10^{-3} volts per channel. Typical spectroscopic systems now often operate with $N = 13$ where $2^{13} = 8{,}192$ channels, with some having $N = 14$, or 16,384 channels.

Although there are a finite number of discrete channels, corresponding to the pulse-height intervals specified in Eq. (6), the peak centroid can occur at any continuous value of h. Thus, it is customary to specify a linear relationship between the continuous values of h and a continuous channel number $\tilde{n}$, given by

$$\tilde{n} = \frac{h - h_{\min}}{\Delta}, \tag{7}$$

which varies continuously between 0 and N. Henceforth, the term channel number is used to mean either the discrete integer channel number n or the continuous channel number $\tilde{n}$; the context can be used to infer the intent.

Detector Response Models

Consider a source that emits photons at a rate with some energy distribution $s(E)$ and a spectrometer that detects the photons and produces a pulse-height spectrum. The basic spectroscopic relationship in its continuous form can be written

$$r(h) = \frac{dR(h)}{dh} = \int_0^\infty s(E)\mathcal{R}(h|E)dE + b(h), \quad h \in [h_{\min}, h_{\max}], \tag{8}$$

where

- $r(h)$ is the detector response such that $r(h)dh$ is the expected number of counts within dh about h per unit time.
- $s(E)$ is the source strength, in photons per unit time, such that $s(E)dE$ is the number of source photons emitted within dE about E.
- $\mathcal{R}(h|E)$ is the detector response kernel such that $\mathcal{R}(h|E)dh$ gives the probability that a particle of energy E interacting in the detector produces a pulse whose height is within dh about h. Here, $\mathcal{R}(h|E) = p(E, E_d)g(h|E_d)$ where $p(E, E_d)dE_d$ is the probability that a source gamma ray of energy E interacts in the detector and deposits an energy in dE_d about E_d in the detector.
- $b(h)$ is the background count rate such that $b(h)dh$ is the expected number of counts within dh about h, per unit time, that are due to background radiation.

Note that $R(h) = \int_0^h r(h')dh'$ is the cumulative number of counts per unit time due to pulses whose heights are less than h and that $R(h_2) - R(h_1) = \int_{h_1}^{h_2} r(h)dh$ is the total number of counts, per unit time, whose pulse heights are between h_1 and h_2. Note also that $\mathcal{R}(h|E)dh$ accounts for the probability of transport of source photons to and within the detector, deposition of energy E_d in the detector, and spreading of the deposited energy into an apparent energy E' that produces a pulse whose pulse height is within dh about h.

In general, a source can emit photons at J discrete energies and also over a continuum of energies. For such sources

$$s(E) = \sum_{j=1}^{J} s_j \delta(E - E_j) + s_c(E), \tag{9}$$

where s_j is the emission rate of photons of energy E_j from the source, $\delta(E - E_j)$ is the Dirac delta function, and $s_c(E)$ is the source emission rate of the photons with a continuum of energies such that $s_c(E)dE$ is the expected number of photons emitted

within dE about E per unit time. For a detector that sorts counts into discrete channels, one can substitute Eq. (9) into Eq. (8), integrate over each channel width, and write the discrete form of the pulse-height spectrum in the form

$$c(n) = \sum_{j=1}^{J} s_j \mathcal{R}_n(E_j) + \int_0^\infty s_c(E)\mathcal{R}_n(E)dE + b_n, \quad n = 1, 2, \ldots, N, \tag{10}$$

where $c(n)$ is the count rate recorded in channel n, b_n is the expected background radiation count rate recorded in channel n, and $\mathcal{R}_n(E)$ is the *detector response function* that is the probability that a particle of initial energy E that is emitted by the source produces a count within the nth channel. Here

$$\mathcal{R}_n(E) = \int_{(n-1)\Delta}^{n\Delta} \mathcal{R}(h|E)\, dh.$$

In general, spectra are accumulated over a counting time $\overline{T}$, in order to increase the number of recorded counts and, hence, improve the statistical precision of the measurements. In this chapter, it is assumed that the source strength $S(E)$ is constant in time. If the photon source is from the decay of a radionuclide, then the measurement time $\overline{T}$ must be much less than the half-life of the radionuclide; otherwise, corrections must be made to correct for the decrease in photon emission rate.

The total counts obtained over counting time $\overline{T}$ per channel can be obtained by integrating Eq. (10) over the counting time. The continuum source term can be due to photons emitted from the source over a continuum of energies and/or to photons emitted at discrete energies from the source that scatter into the detector from material around the detector. Because the primary objective of spectroscopy is to find the E_j and s_j, for $j = 1, 2, \ldots, J$, it is customary to combine the continuum and background terms into a generalized background. Doing so and integrating over the counting time $\overline{T}$, corrected for dead time effects, one obtains

$$\boxed{C(n) = \sum_{j=1}^{J} S_j \mathcal{R}_n(E_j) + B(n), \quad n = 1, 2, \ldots, N,} \tag{11}$$

where $C(n) \equiv C_n = c(n)\overline{T}$ is the detector response in channel n, $S_j = s_j\overline{T}$, and

$$B(n) = \left[\int_0^\infty s_c(E)\mathcal{R}_n(E)dE + b(n)\right]\overline{T}. \tag{12}$$

A plot of $C(n)$ versus n is called a *pulse-height spectrum*. Summation over any range of channels gives the total counts within those channels.

Equation (11) describes an inverse problem, in which the specific E_j and S_j, $j = 1, 2, \ldots, J$ are sought given $J \leq N$ measured pulse-height responses $C(n)$. The generalized background B_n is typically not known explicitly and, thus, further complicates the inversion process. There are different methods that can be used to approach this inverse problem, and the number M of channels, $M \leq N$, used depends on the method chosen. Because most spectrometers have thousands of channels, most spectroscopy inverse problems are overdetermined in the sense that there are considerably more responses available than unknowns.

It is noted that a variant of this inverse problem often is posed in terms of the $k = 1, 2, \ldots, K$ nuclides present in a sample, each of which can emit photons at one or more discrete energies. Rather than look for the J discrete energies and their intensities, one looks for the K nuclides and their concentrations. The form of this inverse problem is similar to the form of Eq. (11) and is defined later more precisely by Eq. (53).

Gamma-Ray Spectroscopy

Suppose that the energy deposition in the detector is that shown in Fig. 2. A simple counter records events in the detector that produced a signal exceeding the lower

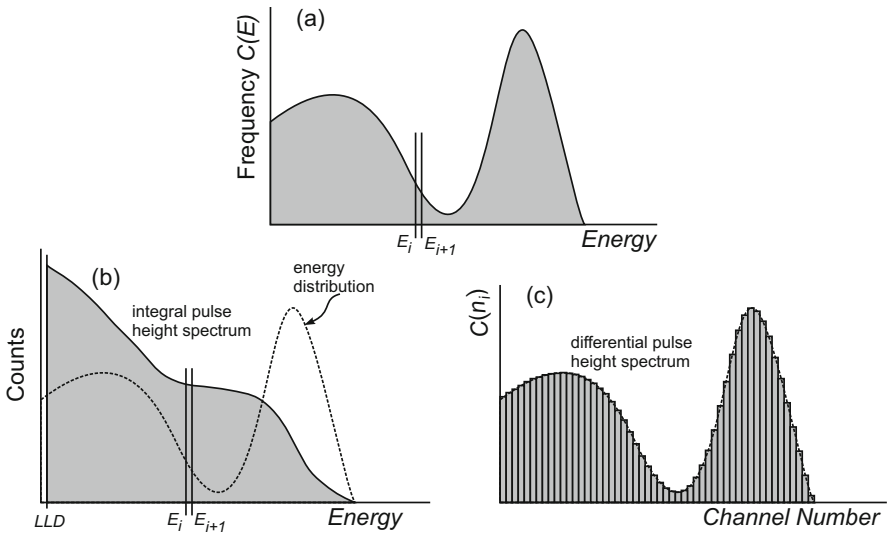

Fig. 2 Shown in (**a**) is the continuous energy distribution recorded with a radiation spectrometer. If a counter is connected to the detector, shown in (**b**) is the resulting count rate as a function of the lower-level discriminator setting, called the integral pulse-height spectrum, superimposed on the radiation energy distribution. Shown in (**c**) is the resulting discrete differential pulse-height spectrum from (**b**). Copyright (2020). From Radiation Detection: Concepts, Methods and Devices by D.S. McGregor and J.K. Shultis. Reproduced by permission of Taylor and Francis Group, LLC, a division of Informa PLC

level discriminator (LLD). In the hypothetical case with no electronic noise or background, *all* events interacting in the detector within measurement time $\overline{T}$ are recorded if the LLD is set to zero. As the LLD is increased, those lower-energy events in Fig. 2a are excluded from the measured count rate, and the total number of recorded counts within time $\overline{T}$ decreases. This function can be plotted as shown in Fig. 2b, where the total integrated counts above the energy equivalent LLD setting are plotted as a function of LLD setting. This plot is called the *integral pulse-height spectrum*. There are notable features in the integral pulse-height curve that can be interpreted as follows: Flatter features indicate energy regions where few events appear, usually from valleys in the energy spectrum. Steeper features indicate energy regions where many counts are located and produce a large change in counts as a function of LLD, often caused by energy maxima or peaks in the energy spectrum.

Although an experienced spectroscopist might be able to interpret the data of an integral pulse-height spectrum, it is usually the derivative of this spectrum that is used in spectroscopy, mainly because interpretation is more straightforward. Suppose the energy spectrum of Fig. 2b is divided into n number of channels, each channel having width of ΔE; then the total number of channels describing the spectrum is

$$n = (E_{\max} - E_0)/\Delta E, \tag{13}$$

where $E_{\max}$ is the highest energy recorded as a function of channel number and E_0 is an experimentally determined *zero offset*. Ideally, the value of E_0 is zero, but in practice usually is not. Suppose that each energy bin is defined by the energies between two adjacent boundaries, i.e., by $E_{i+1} - E_i = \Delta E$. Then the number of counts within each boundary, or channel n, is described by

$$C_i = \int_0^{\infty} C(E)dE - \int_0^{E_i} C(E)dE - \int_{E_{i+1}}^{\infty} C(E)dE = \int_{E_i}^{E_{i+1}} C(E)dE. \tag{14}$$

This result is the same as that found by taking the difference between the counts at E_i and E_{i+1} in Fig. 2b. If this change in the recorded counts from the integral pulse-height spectrum is plotted as a function of the channel number (or energy), then a discrete *differential pulse-height spectrum* is produced

$$C(n_i) = \frac{-(C_{E_{i+1}} - C_{E_i})}{E_{i+1} - E_i} = \frac{-\Delta\text{Counts}}{\Delta E}, \tag{15}$$

as depicted in Fig. 2c.

Figure 2c is a histogram called the *differential pulse-height spectrum*, which mimics the energy distribution seen by the detector, i.e., that of Fig. 2a. For a good spectrometer, the measured energy distribution is very similar to the actual distribution of energy deposited in the detector. However, for detectors that have nonlinear effects, recombination, or charge carrier-trapping problems, the energy deposited in the detector and the output signal are not necessarily proportional.

Although a spectrum such as that depicted in Fig. 2c can be developed with a single-channel analyzer by sequentially moving the energy window ΔE from zero up to 10 volts, it is a multichannel analyzer that is generally used to display the energy spectrum.

Gamma-Ray and x Ray Spectral Features

There are various ways that photons interact in a material and, for the present application, in radiation detectors. The three main mechanisms are the photoelectric interactions, Compton scattering, and pair production. Although Raleigh (coherent) scattering can be significant at low energies, the photoelectric effect dominates (in the same energy region), usually by more than an order of magnitude. Consequently, Rayleigh scattering is usually ignored in practical gamma-ray spectroscopy. Likewise, binding effects become apparent only at low energies and are also usually ignored.

Photoelectric Effect Features

Photons of relatively low energy (less than a few hundreds of keV) interact with the ambient medium mostly through photoelectric absorption in which all of the photon energy is transferred to a bound electron, producing a photoelectron that has kinetic energy

$$T_{pe} = E_\gamma - E_b, \tag{16}$$

where E_b is the binding energy of the electron which depends on its electron shell of origin. The liberated photoelectron moves through the detector medium causing more ionization through Coulombic interactions. Ultimately, an average number of electrons per unit energy are liberated (or excited) in the detector medium. For scintillators, the important quantity is the average number of excited electrons that produces fluorescent light. For gas detectors, the important quantity is the average energy required to produce an electron-ion pair. Similar to gas detectors, in a semiconductor, it is the average energy required to produce an electron-hole pair that is important. Ultimately, the number of information carriers is a function of the average energy w required to produce the carriers and the absorbed photon energy. The photoelectric effect is observed as a *photopeak* in the differential pulse-height spectrum.

Compton Scattering Features

At higher photon energies, ranging between tens of keV and several MeV, depending on the material, the Compton scattering effect becomes dominant compared to the photoelectric effect. The energy of a Compton-scattered electron is

$$T_{cs} = \frac{E_\gamma^2(1-\cos\theta_s)}{m_e c^2 + E_\gamma(1-\cos\theta_s)}, \tag{17}$$

where θ is the photon scatter angle and $m_e c^2 = 511.0\,\text{keV}$ is the rest-mass energy equivalent of an electron. The scattered gamma rays have a continuum of energies from zero up to the maximum possible energy transfer to a Compton electron (for a single scatter at $\theta_s = \pi$), namely

$$T_{cs} = \frac{2E_\gamma^2}{m_e c^2 + 2E_\gamma}. \tag{18}$$

A simple example is the case in which there is a single Compton scatter and the scattered gamma ray escapes the detector. Under such a condition, the energy absorbed by the detector is given by Eq. (17). Consequently, the pulse-height spectrum is a continuum of energies, termed the *Compton continuum*, from zero up to the energy described by Eq. (18). The high-energy limit of the Compton continuum is called the *Compton edge*. If a considerable fraction of photons are Compton-scattered multiple times, ultimately terminating with photoelectric absorption, then the total initial photon energy is represented by the energy peak in the pulse-height spectrum. Because more than one type of interaction contributed to the energy absorption, the proper term for this peak is the *full-energy peak*. A gap appears between the full-energy peak and the Compton edge, termed the *Compton gap*. Multiple Compton scatters that still result in some energy escaping the detector produce a small continuum in the Compton gap. Ultimately, the Compton continuum is more prominent in small detectors than large detectors, mainly because more Compton-scattered photons escape the smaller detector.

Backscatter Features

Compton scattering of source photons in the surroundings and shielding of a detector can result in some of these scattered photons reaching the detector and being absorbed in it. Theoretically, this backscatter spectrum can have energies described by

$$E_{bs} = \frac{E_\gamma m_e c^2}{m_e c^2 + E_\gamma(1-\cos\theta)}, \tag{19}$$

where θ is the scattering angle needed for the scattered photon to reach the detector. The minimum energy of these scattered photons that reach the detector occurs when $\theta = \pi$ and is

$$E_{bs} = \frac{E_\gamma m_e c^2}{m_e c^2 + 2E_\gamma}. \tag{20}$$

Forward scattering of gamma rays becomes more probable with increasing gamma-ray energy. Hence, the differential backscatter cross section actually decreases with higher gamma-ray energies. However, photons that scatter with angle greater than about 100° emerge with nearly the same energies.

Pair Production Features

If the gamma-ray energy is greater than 1.022 MeV, then pair production is possible. When this photon interaction occurs in a detector, 1.022 MeV of the photon energy is converted into the masses of the electron-positron pair and the remaining energy shared as kinetic energy between the two particles. The particles produce ionization in the detector just like photoelectrons and Compton electrons. After the electron loses almost all its initial energy, it is absorbed in the material and returns to an allowed state. However, when the positron comes to rest, it combines with an electron and annihilates, producing two 511-keV photons emitted in opposite directions to preserve the zero linear momentum condition. If both of the annihilation photons are reabsorbed in the detector, the initial gamma-ray energy is represented in the full-energy peak. If multiple events result in one 511-keV annihilation photon escaping the detector, then an energy peak forms in the pulse-height spectrum at $E_\gamma - 511$ keV, named a *single-escape peak*. If multiple events result in both 511-keV annihilation photons escaping the detector, then an energy peak forms in the pulse height spectrum at $E_\gamma - 1.022$ MeV, named a *double-escape peak*. Single- and double-escape peaks can be identified by (1) noticing that no Compton edge forms and (2) noting their energy location with respect to the full-energy peak. Escape peaks are more prominent in small detectors than large detectors, mainly because a larger fraction of annihilation photons escape the smaller detector.

Fluorescent X Ray Features

As described previously, the initial liberated electrons, be it by photoelectric, Compton scattering, or pair production, lose energy through Coloumbic interactions which produce secondary electron ionization (delta rays). Some electrons are completely liberated, while others are excited to various higher-energy levels. During this energy transfer process, it is possible for de-exciting electrons to release characteristic x rays. If interaction events occur near the surface of a detector, then these characteristic x rays may escape and produce what is called an "x ray escape peak" correlating to the detector material. In a similar fashion, gamma rays can also fluoresce the shielding and detector surroundings, producing a background of characteristic x rays that appear as peaks in the pulse-height spectrum. Often common shielding materials, such as Pb and Cu, will introduce characteristic x ray peaks into the lower-energy region of a pulse-height spectrum.

Summary

To summarize, consider a radiation source that emits monoenergetic photons of energy E_o. A source photon that enters the detector may experience any of several outcomes, including the following:

1. It may be completely absorbed by photoelectric absorption, in which case the deposited energy is the photon energy, i.e., $E_d = E_o$.
2. It might undergo a sequence of one or more scatters within the detector and then be absorbed within the detector by photoelectric absorption. Full-energy absorption again leads to $E_d = E_o$.
3. It might scatter one or more times in the detector and then escape with an energy E_r. Because not all of the gamma-ray energy is deposited, the recorded energy will be $E_d = E_o - E_r$.
4. If $E_o > 1.022$ MeV, it might undergo pair production in the detector, producing an electron-positron pair that usually leads to the production of two 0.511-MeV photons by positron annihilation. If both annihilation photons deposit all of their energy in the detector, then $E_d = E_o$. If one of the annihilation photons escapes and the other is absorbed, the energy deposited is $E_d = E_o - 0.511$ MeV. If both annihilation photons escape the detector, the deposited energy is $E_d = E_o - 1.022$ MeV. If either or both annihilation photons scatter within the detector and then escape, an intermediate energy within the range $E_o - 1.022 < E_d < E_o$ is deposited.
5. It might not interact at all in the detector and so $E_d = 0$.

Note that outcomes 1 and 2 both contribute to a "full-energy" peak. Voltage pulses will result whose pulse heights are distributed from zero up to a maximum determined by the energy E_d and the energy resolution of the detector. Thus, a monoenergetic source produces a pulse-height spectrum that is distributed over the many channels. These features can be combined to produce the expected features that appear in a gamma-ray pulse-height spectrum. Depicted in Fig. 3 are differential pulse-height spectra for monoenergetic gamma rays with energies below and above 1.022 MeV.

An example pulse-height spectrum obtained from a scintillation spectrometer exposed to the photons from a ^{22}Na source, which emits 1.28-MeV photons and 0.511-MeV annihilation photons, is shown in Fig. 4. The features in the spectrum, from right to left, include a full-energy peak centered about the channel corresponding to $E_1 = 1.28$ MeV, a Compton edge and a continuum extending from about channel 1250 downward, a full-energy peak due to 0.511-MeV annihilation photons, a Compton edge and Compton continuum for the annihilation photons, and a backscatter peak. The maximum amount of energy that a photon can give up in a Compton scatter occurs in a "backscatter" through an angle of π radians, and so the Compton edge occurs over those channels that represent Compton scatters in the detector through angles near π. Photons that are emitted by the source and backscatter (within either the source or the material behind the source) have energies that are near the energy given by Compton scatter through π radians. The backscatter peak in the spectrum of Fig. 4 is caused by source gamma rays that scatter, in or near the sample, through angles close to π and then deposit full energy in the detector. This peak typically has an FWHM that is larger than the FWHM of a full-energy peak for monoenergetic photons. The larger FWHM occurs because source photons can backscatter in or near the source over a range of angles near π

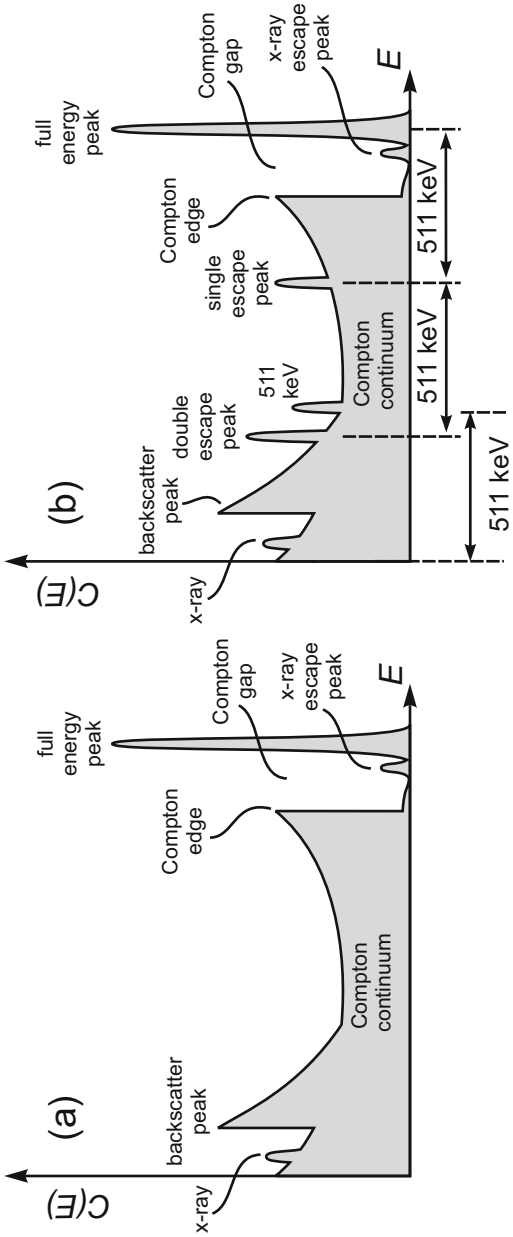

Fig. 3 Composite pulse-height spectra for monoenergetic gamma rays formed from the features described in this section, with (**a**) $E_\gamma < 1.022$ MeV and (**b**) with $E_\gamma > 1.022$ MeV. Copyright (2020). From Radiation Detection: Concepts, Methods and Devices by D.S. McGregor and J.K. Shultis. Reproduced by permission of Taylor and Francis Group, LLC, a division of Informa PLC

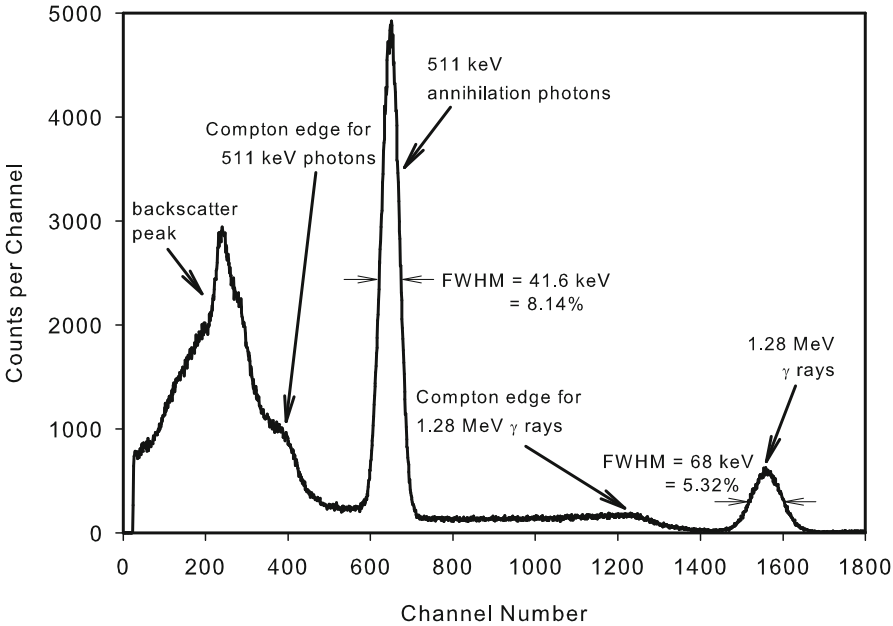

Fig. 4 The pulse-height spectrum obtained by an NaI(Tl) scintillation detector exposed to a ^{22}Na source. The source emits photons at 0.511 MeV, as a result of positron annihilations, and at 1.28 MeV, emitted as the product ^{22}Ne transitions from the excited state to the ground state [McGregor 2016]

radians, and thus these scattered photons that reach the detector do not all have the same energy.

Spectral Response Function

A spectrum such as that in Fig. 4, normalized to unit concentration, is called the *spectral response function* for a given radionuclide. Each nuclide has a characteristic detector response function for each spectrometer for a specified source-detector geometry. Let the subscript k refer to a specific nuclide. Then the detector response function u_{nk} is the expected response (number of counts) of the spectrometer in channel n per unit concentration of nuclide k.

Detector response functions also can be associated with monoenergetic photons. If a source of monoenergetic photons of energy E_j, in some specific source-detector geometry, irradiates a detector, then the detector response function u_{nj} gives the expected response in channel n per source particle of energy E_j emitted from the source. In either case, it is not only the full-energy peaks that are of interest; the entire spectrum contains information about the source. Ways to exploit this fact are considered later.

Qualitative Analysis

For some purposes, it is necessary to identify only whether or not a sample emits photons at certain discrete energies E_j. This may be the case, for instance, if one wants to know if a sample contains a particular radionuclide. Alternatively, a procedure such as EDXRF, NAA, or PGNAA can be used to excite characteristic photons from a sample under investigation. If the element of interest is present, the characteristic photons emitted from the sample should create full-energy peaks in a pulse-height spectrum collected from the sample.

Photons of energy E_j that are emitted by the source produce full-energy pulses whose magnitudes are distributed about a mean value of

$$h_j = f(E_j). \tag{21}$$

A pulse of magnitude h_j produces a count in discrete channel n_j if

$$h_{\min} + (n_j - 1)\Delta < h_j \leq h_{\min} + n_j\Delta.$$

For purposes of energy determination, it is useful to consider the continuous, non-integer, channel number n_j corresponding to the pulse-height h_j of the full-energy peak. Then the gamma-ray energy can be estimated by determining the continuous or fractional channel number $\tilde{n}_j$ centroid of each peak.

It is then straightforward to obtain the corresponding h_j from

$$h_j = h_{\min} + \tilde{n}_j\Delta. \tag{22}$$

For the usual case, where $h_{\min} = 0$ and $h_{\max} = 10\,\text{V}$, this reduces to

$$h_j = \frac{10}{N}\tilde{n}_j. \tag{23}$$

The expected source energy is then easily obtained from

$$E_j = f^{-1}(h_j). \tag{24}$$

For a linear detector whose response is given by Eq. (2), then Eq. (24) is simply

$$E_j = \frac{h_j - \alpha}{\beta}. \tag{25}$$

If a nuclide emits several characteristic-energy photons, then one can gain confidence in the conclusion that the element is present if peaks occur at all energies for which the photon abundance and the detection efficiency would lead one to suspect that a peak should occur.

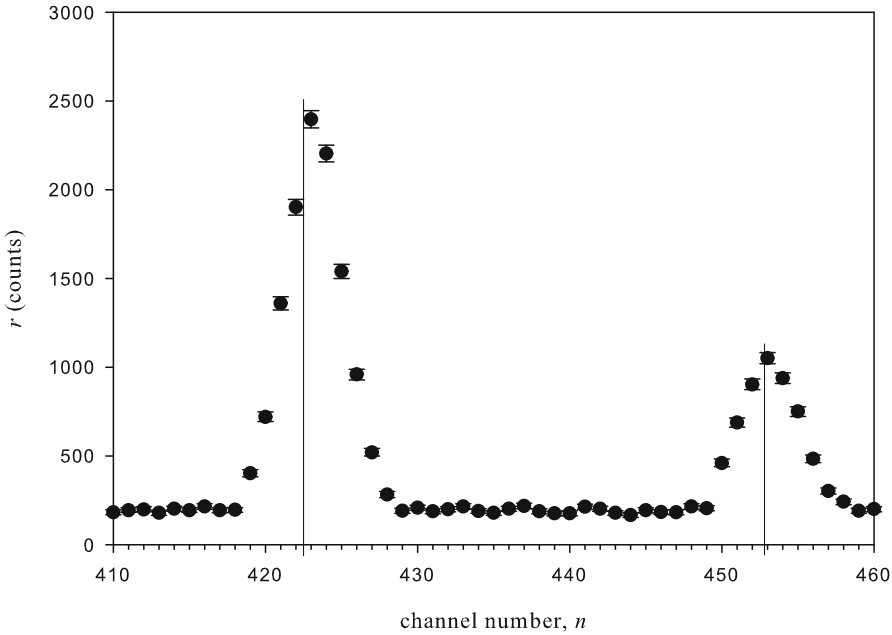

Fig. 5 An example of visual inspection to yield the channel numbers corresponding to the centroids of two peaks in a spectrum. The vertical lines are used to connect the apparent peaks to their centroid channel numbers

The simplest way to estimate the channel corresponding to the peak is by inspection of the plotted spectrum. This technique often is adequate. One merely estimates the continuous channel number $\tilde{n}_j$ that corresponds to the apparent centroid of the full-energy peak due to photons of energy E_j. For instance, in the spectrum shown in Fig. 5, one can obtain estimates of the fractional channel numbers of the centroids of the two peaks shown. It should be apparent that this procedure is subjective (different researchers may estimate slightly different centroids) and, thus, has limited accuracy. Nevertheless, this procedure may suffice for some applications.

When estimation of the centroid by inspection is deemed insufficient, other methods must be employed. The wavelet transform has been used in various spectroscopic applications, including nuclear magnetic resonance (Barache et al. 1997) and Raman spectroscopy (Xu et al. 1994). However, this approach is not commonly employed in gamma-ray spectroscopy and, thus, is not further considered here. Rather, it is common that the centroids of the peaks present are identified as part of a fitting process that can determine quantitative information about both the characteristic energies E_j and their relative abundances. Alternatively, such methods may seek to identify particular radionuclides and their concentrations in a sample. Such methods are discussed in the next sections.

Quantitative Analysis

The model of Eq. (11) identifies a general inverse problem in which many channels contain information about the source distribution. One typically seeks to determine not only the characteristic energies E_j emitted by the source but also the individual source strengths s_j from the measured responses. Alternatively, one may use the spectral responses to identify the nuclide k and its concentration ξ_k in a sample. Quantitative analysis refers to the determination of quantities such as s_j and ξ_k. There are several approaches to quantitative analysis in spectroscopy, including the following:

1. Area under isolated peaks
2. Model fitting
3. Spectrum stripping
4. Library least-squares
5. Symbolic Monte Carlo

Summaries of how these methods are typically implemented are given in the following sections. In general, one seeks to obtain both the E_j, $j = 1, 2, \ldots, J$, and the net areas under each of the J peaks. For spectra that are linearly related to the source strengths, the net area A_j under the jth full-energy peak is related to S_j, the number of gamma rays emitted by the source during the counting time $\overline{T}$, by

$$S_j = \frac{A_j}{\eta_j},$$

where η_j is the detector efficiency, presumed known, at energy E_j,

$$A_j = \sum_{n_1}^{n_2} [C(n) - B(n)], \tag{26}$$

and n_1 and n_2 are channel numbers over which the peak is spread. Similarly, in linear systems, the concentration ξ_k of nuclide k is directly related to the net peak area.

A gamma-ray spectrum, generally, consists of a series of peaks atop a continuum produced by sources emitting a continuum of energies and Compton plateaus from scattered photons. Ideally such a spectrum can be described by a sum of K Gaussian peaks plus a continuum as

$$y(n) = \sum_{k=1}^{K} g_k(n, \mu_k, \sigma_k) + B(n), \tag{27}$$

where

$$g_k(\tilde{n}, \mu_k, \sigma_k) = \frac{A_k}{\sqrt{2\pi}\sigma_k} \exp\left[-(\tilde{n} - \mu_k)^2/(2\sigma_k^2)\right] = B_k \exp\left[-((\tilde{n} - \mu_k)/\tau_k)^2\right]. \tag{28}$$

Here, $A_k = \sqrt{\pi}\tau_k B_k$ is the number of counts in peak k and $\sigma_k = \tau_k/\sqrt{2}$ is the standard deviation of the peak. Usually, the continuum is represented by a (piecewise) polynomial of $\tilde{n}$ of low order. The principal purpose of quantitative analysis of the spectrum is to determine values of A_k and μ_k from which radioisotope identification and concentrations can be determined. Also in calibrated MCA spectrometer systems, the continuous channel number $\tilde{n}$ is replaced by the photon energy E and the channel number n by the energy E_n at the channel midpoint.

Area Under an Isolated Peak

For isolated peaks, i.e., those that do not overlap with other peaks, a simple approach can be used to estimate the net peak area. Generally, the peak is superimposed on a generalized background, as shown, for an ideal case, in Fig. 6. To obtain the net area A, one identifies the channel numbers, n_1 and n_2, at which the peak disappears into the background. Then, the net peak area is estimated as

$$A = \sum_{n=n_1}^{n_2} C(n) - \left[(n_2 - n_1)\frac{C(n_1) + C(n_2)}{2}\right]. \tag{29}$$

The net area is the total number of counts between channels n_1 and n_2 minus the area under an (assumed) linear background between $C(n_1)$ and $C(n_2)$. For instance, for the spectrum shown in Fig. 6, one might choose $n_1 = 833$ and $n_2 = 861$. The total area between these channels is the sum of the counts in each channel, and the background is the area under the straight line connecting $C(833)$ and $C(861)$; thus, the net area A is the area beneath the peak and above the background line in the figure.

This simple procedure cannot be applied to overlapping peaks and gives only approximate net areas because the background may not be linear under the peak and identifying the channels n_1 and n_2 is subjective, especially when the standard deviations of the responses, $\sigma(C(n_1))$ and $\sigma(C(n_2))$, are large relative to the values $C(n_1)$ and $C(n_2)$.

Model Fitting

A second technique, which can be used to obtain both the peak centroid and the area under the peak, is to fit a model to the data. Each peak is modeled as consisting of a peak function and a background function. In most gamma-ray spectroscopy applications, the peak function is assumed to be the product of a magnitude and a Gaussian PDF. Because the integral of the Gaussian PDF is unity, the magnitude

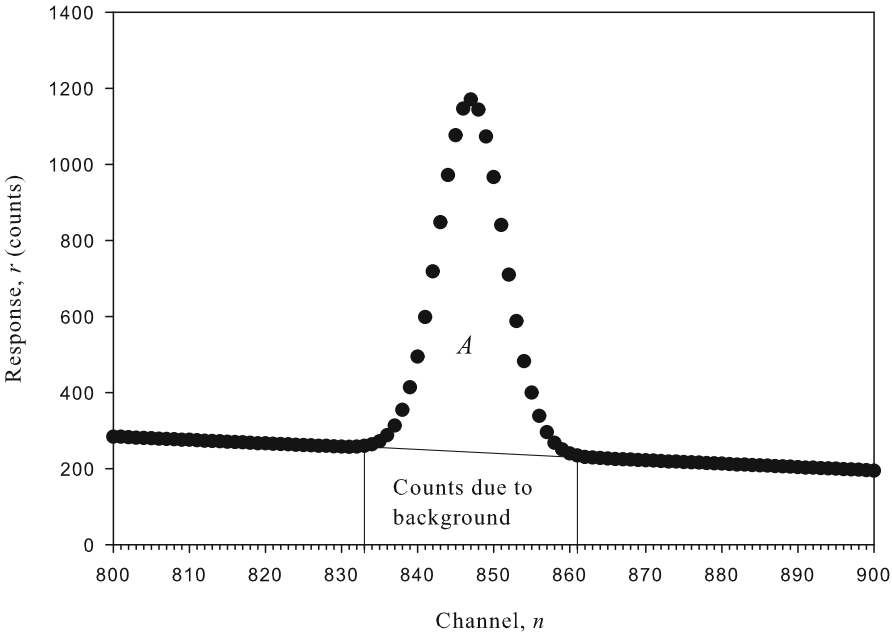

Fig. 6 The net area A under the peak but above background

is just the desired net peak area. The background can be assumed to have any functional form but most often is assumed to be a polynomial. As a rule of thumb, there is little extra work in treating the background function as quadratic (or even cubic) as opposed to linear, and better results are generally obtained if this is done. If the best fit occurs for a linear background function, the coefficients of the higher-order terms are determined to be zero (or very small); if not, then appropriate coefficients for the higher-order terms assume appropriate values. Note that the background model is not physically based but is empirical. Nevertheless, this model-fitting approach works quite well, for both isolated and overlapping peaks.

General Linear Least-Squares Model Fitting

Here is considered the problem of fitting a linear combination of M *basis functions* $X_k(x)$ to a set of data points (x_i, y_i), i.e.,

$$y(x|a_1, \ldots, a_M) \equiv y(x|\mathbf{a}) = \sum_{m=1}^{M} a_m X_m(x), \tag{30}$$

where $X_m(x)$ can be highly nonlinear in x. The term "linear" refers to the linear dependence of the model on the parameters a_m. This problem is a more general

problem of fitting a straight line to a set of data in which $X_1(x) = 1$ and $X_2(x) = x$. As before, one seeks values of the parameters a_m that minimize the merit function:

$$\chi^2 = \sum_{i=1}^{N} \left[\frac{y_i - \sum_{m=1}^{M} a_m X_m(x_i)}{\sigma_i} \right]^2. \tag{31}$$

First define an $N \times M$ *design* matrix $\mathbf{A}$ with elements

$$A_{ij} = \frac{X_j(x_i)}{\sigma_i}. \tag{32}$$

In general $N \geq M$ because there must be at least as many data points as there are model parameters. Also define a vector $\mathbf{b}$ with components

$$b_i = \frac{y_i}{\sigma_i}, \quad i = 1, \ldots, N, \tag{33}$$

and a vector $\mathbf{a}$ whose components are the parameters a_m, $m = 1, \ldots, M$.

The minimum of χ^2 occurs when $\partial\chi^2/\partial a_m = 0$ or when

$$0 = \sum_{i=1}^{N} \frac{1}{\sigma_i^2} \left[y_i - \sum_{j=1}^{M} a_j X_j(x_i) \right] X_m(x_i), \quad m = 1, \ldots, M. \tag{34}$$

This is a set of M linear algebraic equations in the M unknown a_m. These so-called normal equations can be written compactly as

$$\sum_{j=1}^{M} \alpha_{mj} a_j = \beta_m, \quad m = 1, \ldots, M, \tag{35}$$

where

$$\alpha_{mj} = \sum_{i=1}^{N} \frac{X_j(x_i) X_m(x_i)}{\sigma_i^2} \qquad \text{or equivalently} \qquad \boldsymbol{\alpha} = \mathbf{A}^T \cdot \mathbf{A}, \tag{36}$$

and

$$\beta_m = \sum_{i=1}^{N} \frac{y_i X_m(x_i)}{\sigma_i^2} \qquad \text{or equivalently} \qquad \boldsymbol{\beta} = \mathbf{A}^T \cdot \mathbf{b}. \tag{37}$$

Equations (35) can be solved by any standard linear equation solver such as Gauss-Jordan or Cholesky decomposition techniques. However, these normal equations are susceptible to roundoff errors, and often these simple solution methods

fail, and more sophisticated methods such as the *singular value decomposition* technique should be used. Formally, the solution of Eq. (35) can be written as

$$a_j = \sum_{m=1}^{M} [\boldsymbol{\alpha}^{-1}]_{jm} \beta_m = \sum_{m=1}^{M} C_{jm} \left[\sum_{i=1}^{N} \frac{y_i X_m(x_i)}{\sigma_i^2} \right], \tag{38}$$

where $\mathbf{C} = \boldsymbol{\alpha}^{-1}$.

However, finding the model parameters is not the end of the data-fitting problem. The standard errors for the estimated parameters must also be estimated. With the usual formula for the propagation of errors, the variance of a fit parameter is estimated as

$$\sigma^2(a_j) = \sum_{i=1}^{N} \sigma_i^2 \left(\frac{\partial a_j}{\partial y_i} \right)^2. \tag{39}$$

Because C_{jm} is independent of y_i, differentiation of Eq. (38) with respect to y_i gives

$$\frac{\partial a_j}{\partial y_i} = \sum_{m=1}^{M} C_{jm} X_m(x_i)/\sigma_i^2, \tag{40}$$

so that

$$\left(\frac{\partial a_j}{\partial y_i} \right)^2 = \frac{1}{\sigma_i^2} \sum_{m=1}^{M} \sum_{k=1}^{M} C_{jm} C_{jk} \left[\sum_{i=1}^{N} X_m(x_i) X_k(x_i) \right]. \tag{41}$$

Substitution of Eq. (41) into Eq. (39) produces

$$\sigma^2(a_j) = \sum_{m=1}^{M} C_{jm} \sum_{k=1}^{M} C_{jk} \left[\sum_{i=1}^{N} \frac{X_m(x_i) X_k(x_i)}{\sigma_i^2} \right] = C_{jj}. \tag{42}$$

The last simplification in this result arises because the term in square brackets is α_{km} (see Eq. (36)), and because $\boldsymbol{\alpha}^{-1} = \mathbf{C}$, one has

$$\sum_{k=1}^{M} C_{jk} \left[\sum_{i=1}^{N} \frac{X_m(x_i) X_k(x_i)}{\sigma_i^2} \right] = \sum_{k=1}^{M} C_{jk} C_{km}^{-1} = [\mathbf{C} \cdot \mathbf{C}^{-1}]_{jm} = \delta_{jm}. \tag{43}$$

Hence, the diagonal elements of the $\mathbf{C}$ matrix are the variances of the estimated parameters. Not surprisingly, the off-diagonal elements of $\mathbf{C}$ are the covariances $\mathrm{covar}(a_j, a_m)$.

Computer programs and subroutines for performing linear least-squares fits are provided by Press et al. (1992), Bevington (1969), and Moré et al. (1980). An

application of this fitting procedure for an isolated peak is given in the following example.

Example 1. Consider a full-energy peak produced in an HPGe spectrometer from 350-keV gamma rays emitted by the naturally occurring ^{214}Pb radionuclide. The measured data in the spectrum around this peak are listed in Table 1. Fit the data to a Gaussian distribution and determine the area of the peak.

Solution 1. From Fig. 7, the data appears to consist of a single Gaussian on top of an almost linear background. Thus, the general model of Eq. (27) reduces to

$$y(E, E_o, \sigma) = \frac{A}{\sqrt{2\pi}\sigma} \exp[-(E - E_o)^2/(2\sigma^2)] + a_1 + a_2 E. \tag{44}$$

It is this model that is to be fitted to the data in Table 1. However, to use the general linear least-squares fitting method described in this section, the peak energy E_o and its standard deviation σ must be known a priori so that the fitting function depends only linearly on A, a_1, and a_2.

Because the radioisotope is given as ^{214}Pb, then the energy of the decay gamma ray shown in Table 1 is $E_o = 351.9$ keV, which, for this example, is rounded to 352 keV. The variances of the counts are taken as the number of counts, i.e., $\sigma_i^2 = y_i$. From past experience with the spectrometer used to obtain the data of Table 1, the value of $\sigma \simeq 0.47$ keV. Thus, it is decided to look at two cases, one in which $\sigma = 0.45$ keV and another in which $\sigma = 0.50$ keV. The results of the fits for the two choices of σ are shown in Fig. 7. Clearly, $\sigma = 0.50$ kev is a better choice.

To determine the number of counts in the peak, the method described in section "Area Under an Isolated Peak" could be used. By inspection, $n_1 = 9$ and $n_2 = 20$. Then the area is

Table 1 A portion of a spectrum around the 351.93-keV ^{214}Pb full-energy peak

i	E_i (keV)	y_i cnts	i	E_i (keV)	y_i cnts	i	E_i (keV)	y_i cnts	i	E_i (keV)	y_i cnts
1	348.3	2626	9	350.4	2651	17	352.6	4927	25	354.8	2303
2	348.5	2574	10	350.7	2969	18	352.9	3561	26	355.1	2457
3	348.8	2594	11	351.0	3669	19	353.2	2888	27	355.3	2388
4	349.1	2588	12	351.3	4952	20	353.4	2461	28	355.6	2433
5	349.4	2558	13	351.5	6388	21	353.7	2417	29	355.9	2310
6	349.6	2579	14	351.8	7701	22	354.0	2399	30	356.2	2477
7	349.9	2658	15	352.1	7931	23	354.3	2550	31	356.4	2385
8	350.2	2650	16	352.4	6735	24	354.5	2405			

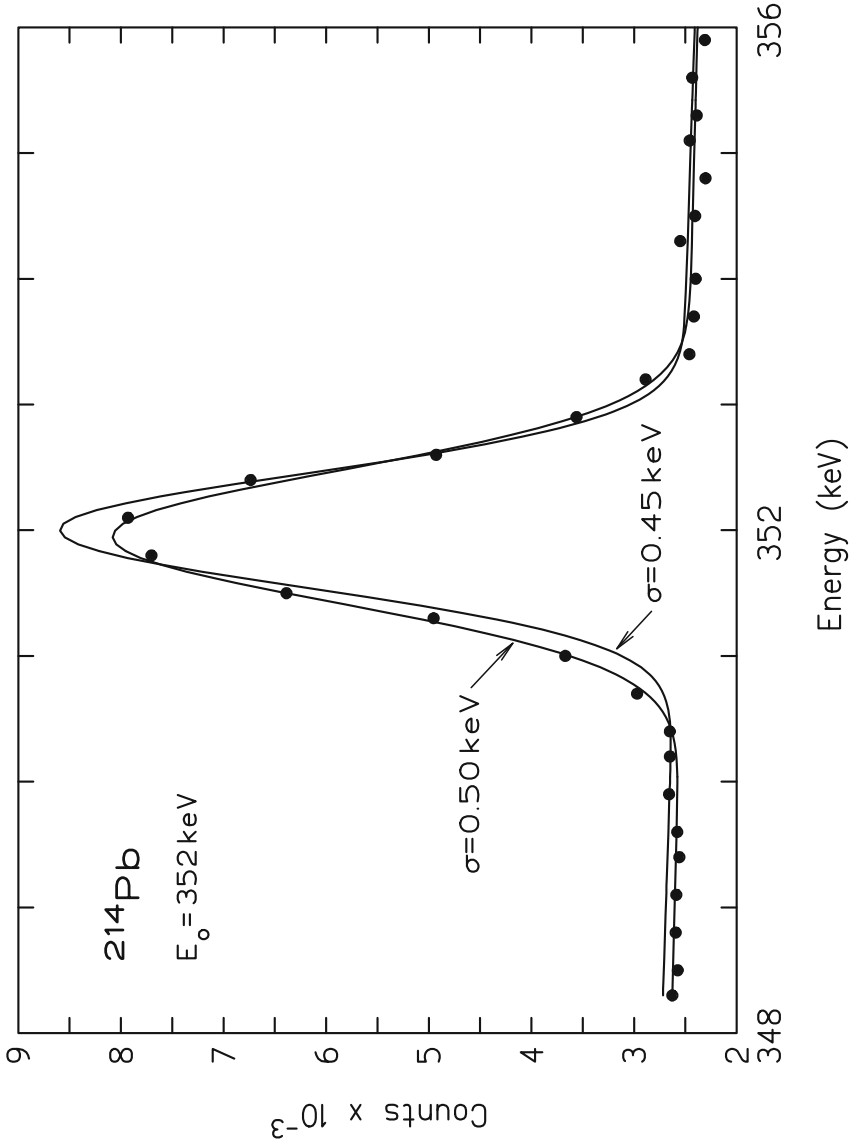

Fig. 7 Two linear least-squares fits of Eq. (44) to the data of Table 1 for two assumed values of σ

$$\text{area}_1 = \sum_{n=9}^{20} c(n) - \text{ trapezoid area}$$
$$= 56,833 - \frac{1}{2}[c(9) + c(20)][11] = 28,717.$$

From the linear least-squares fit (with $E_o = 352\,\text{keV}$ and $\sigma = 0.50$), it is found that $A = 7161.79 \pm 62.19\,\text{keV}$, $a_1 = 15819 \pm 1316$, and $a_2 = -37.75 \pm 3.73\,\text{keV}^{-1}$. The energy width per channel is

$$\Delta E = \frac{E(31) - E(1)}{31 - 1} = 0.2700\text{keV/ch}.$$

Thus, the least-squares area of the Gaussian peak is estimated as

$$\text{area}_2 = [A \pm \sigma(A)]/\Delta E = \frac{7161.79 \pm 62.188\text{keV}}{0.2700\text{keV}} = 26,525 \pm 230.$$

Nonlinear Least-Squares Model Fitting

Often the model $y(x|\mathbf{a})$ to be fitted to the data $y_i,\ i = 1, ..., N$ depends both linearly on some of the parameters in $\mathbf{a}$ and nonlinearly on the remaining M parameters. As before, in the least-squares method, values of the parameters are determined by choosing parameter values that minimize the merit function:

$$\chi^2(\mathbf{a}) = \sum_{i=1}^{N} \left[\frac{y_i - y(x_i|\mathbf{a})}{\sigma_i} \right]^2. \tag{45}$$

The normal equations (similar to Eq. (34)) are no longer linear in the parameters $\mathbf{a}$ and so cannot be solved directly. Rather, iterative techniques must be used to find the minimum of $\chi^2(\mathbf{a})$.

Equation (45) describes a hypersurface in the M-dimensional hyperspace whose axes are the M parameters in $\mathbf{a}$. One must incrementally traverse this hypersurface in some methodical fashion to find its minimum. Such searches range from brute-force grid searches, in which one moves incrementally along each axis to find a local minimum before searching along another axis, to more sophisticated searches, in which each incremental step is taken in a direction opposite to the gradient of $\chi^2(\mathbf{a})$. However, the hypersurface often has many local minima in which an incremental search can become trapped and thus miss the sought-for global minimum. Moreover, these searches can often venture into regions of the hyperspace with physically unrealistic parameter values, such as those producing negative Gaussian distributions. Such a problem is frequently encountered if a search is begun far from the global minimum. Consequently, it is often necessary to do a

constrained search to prevent the search path from entering unrealistic regions of the hyperspace.

In the analysis of gamma-ray spectroscopic data (x_i, y_i), x_i is either the channel number n or the channel midpoint energy E_n, and y_i is the measured number of counts in a channel. Typically, data in a gamma-ray spectrum or, more often, a portion of the spectrum are fit to a sum of Gaussian peaks plus a polynomial to represent the continuum upon which the peaks sit. For this case, the fitting model is

$$y(x|\mathbf{a}) = \sum_{k=1}^{K} B_k \exp\left[-\left(\frac{x - E_k}{\tau_k}\right)^2\right] + a_0 + a_1 x + a_2 x^2 + \ldots + a_n x^n. \quad (46)$$

The model parameters $B_1,\ E_1,\ \tau_1, \ldots, B_K,\ E_K,\ \tau_K,\ a_0,\ a1, \ldots, a_n$ are the components of $\mathbf{a}$. However, other models are easily treated with the nonlinear least-squares technique described below.

There are several ways to search the M-dimensional hyperspace to find $\mathbf{a}_{\min}$ that minimizes $\chi^2(\mathbf{a})$ of Eq. (45). One such method is the Leverberg-Marquardt (LM) method, such as that presented by Press et al. (1992). McGregor and Shultis (2020) also describe the method as applied to gamma-ray spectroscopy. The reader is referred to these two citations for a review of the technique.

Isolated Peaks

To assure that the entire isolated peak is completely fit, it is suggested that the portion of the spectrum extend to at least $\pm 3\sigma$ about the centroid channel. These limits are chosen because the area under a Gaussian over the range $\mu \pm 3\sigma$ is 0.997 of the total area under the Gaussian, and thus the parameter A_k in Eq. (28) is a very good approximation to the total area under the Gaussian for the kth peak.

For the portion of the spectrum containing an isolated peak, the appropriate fitting model $y(x|\mathbf{a})$ is that of Eq. (27) with $K = 1$ and a polynomial of low order n to describe the background upon which the peak sits. The merit function to be minimized in this case is

$$\begin{aligned}\chi^2(\mathbf{a}) &= \sum_{i=1}^{N} \left[\frac{y_i - y(x_i|\mathbf{a})}{\sigma_i}\right]^2 \\ &= \sum_{i=1}^{N} \frac{1}{\sigma_i^2}\left[y_i - \left\{B \exp\left[-\left(\frac{x_i - \mu}{\tau}\right)^2\right] + \sum_{m=0}^{n} a_m x_i^m\right\}\right]^2, \end{aligned} \quad (47)$$

where the components of the parameter vector $\mathbf{a}$ are $B,\ \mu,\ \tau,\ a_0, \ldots, a_n$. To use the LM method, the derivatives of $y(x|\mathbf{a})$ with respect to each parameter are needed. Here one has

$$\frac{dy(x|\mathbf{a})}{dB} = f(x, \mu, \tau), \qquad \frac{dy(x|\mathbf{a})}{d\mu} = Bf(x, \mu, \tau)\frac{2(x - \mu)}{\tau^2},$$

$$\frac{dy(x|\mathbf{a})}{d\tau} = f(x,\mu,\tau)\frac{2(x-\mu)^2}{\tau^3}, \quad \text{and} \quad \frac{dy(x|\mathbf{a})}{da_j} = x^j, \quad j = 0, 1, ..., n. \quad (48)$$

To illustrate this analysis approach, the data of Table 1 for a ^{214}Pb peak are fit to a Gaussian plus a linear function ($n = 1$) in Example 2.

Example 2. For the portion of a spectrum containing an isolated peak, as given by the data in Table 1, the fitting model $y(x|\mathbf{a})$ is given by Eq. (46) with $K = 1$ and a linear background function, so $n = 1$ in Eq. (46). This is the same model used in Example 1, but now estimate the centroid of the peak and its standard deviation by including them in the fitting parameters.

Solution 2. The merit function to be minimized is that of Eq. (47) with $n = 1$. The initial guess of the parameter values was

$$B = 3000 \text{ MeV}, \quad \mu = 0.350 \text{ MeV}, \quad \tau = 0.002 \text{ MeV},$$
$$a_0 = 1000, \quad a_1 = -200 \text{ MeV}^{-1}.$$

After 23 LM steps through 5-dimensional parameter hyperspace, the $\chi^2(\mathbf{a})$ was reduced from an initial value of 16,653 to 72.55, the minimum of $\chi^2(\mathbf{a})$. The best-fit parameters at the $\chi^2(\mathbf{a})$ minimum were

$$B = 5583.6 \pm 58.4, \quad \mu = 351.960 \pm 0.0051 \text{ keV}, \quad \tau = 0.74146 \pm 0.00744 \text{ keV},$$
$$a_0 = 14062 \pm 1331 \quad \text{and} \quad a_1 = -32823 \pm 3776 \text{ MeV}^{-1}$$

The normalization of the Gaussian is $A = \sqrt{\pi}\tau B = 7338.0 \pm 70.64$ keV counts/channel, which, upon dividing by the energy width per channel of 0.2700 keV/channel, gives the total counts in the peak as

$$\text{area}_3 = 27,178 \pm 262.$$

This result is midway between the two estimates $\text{area}_1 = 28,717$ and $\text{area}_2 = 26,525 \pm 230$ obtained in Example 1. Finally, the standard deviation of the peak is $\sigma = \tau/\sqrt{2} = 0.52429 \pm 0.00526$ keV. The resulting model fit and its two components are shown in Fig. 8. Of note is the estimated gamma-ray energy of 351.960 keV for this peak. This value compares very favorably to the accepted NUDAT value of 351.9321(18) keV. The small difference is easily accounted for by inevitable small errors in the energy calibration of the channels of the spectrometer system.

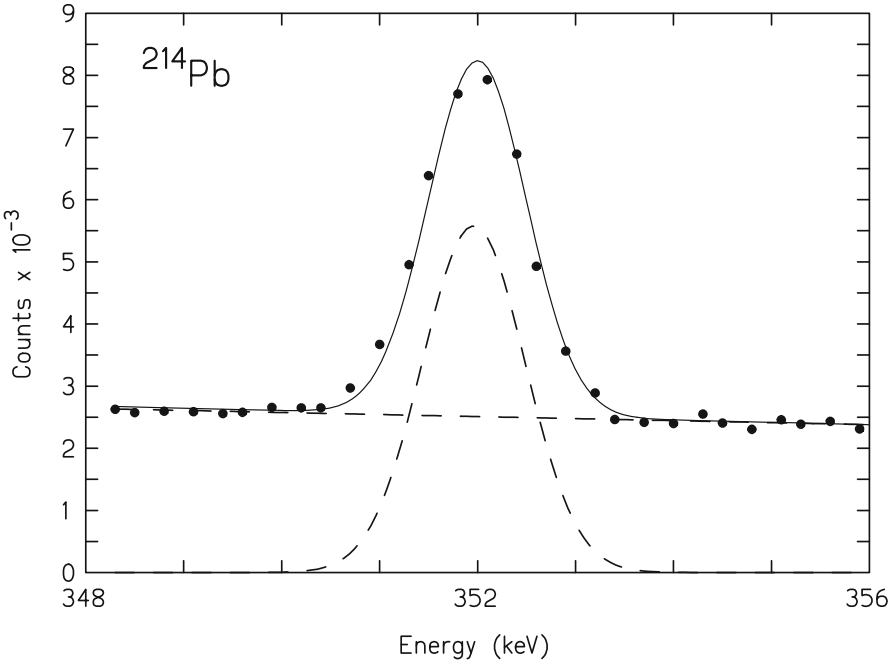

Fig. 8 The LM fit to the data of Table 1. Also shown by dashed lines are the Gaussian peak component and the linear background

Overlapping Peaks

Sometimes two or more peaks overlap. In situations where a peak is asymmetric or has an FWHM larger than expected, one can try to fit multiple peaks to the data locally. In such cases, one might try a fitting model of the form (see Eq. (27))

$$y(x|\mathbf{a}) = \sum_{j=1}^{K} B_j g_j(x, \mu_j, \tau_j) + a_0 + a_1 x + a_2 x^2,$$

$$\text{where } \; g(x, \mu_j, \tau_j) = \exp\left[-\left(\frac{x - \mu_j}{\tau_j} \right)^2 \right], \tag{49}$$

and K is the number of peaks one suspects might be overlapping.

Values of the model parameters $\mathbf{a} = (B_1, \mu_1, \tau_1, \ldots, B_K, \mu_K, \tau_K, a_0, a_1, a_2)$ are found as those values that minimize the merit function:

$$\chi^2(\mathbf{a}) = \sum_{i=1}^{N} \left[\frac{y_i - y(x_i|\mathbf{a})}{\sigma_i} \right]^2$$
$$= \sum_{i=1}^{N} \frac{1}{\sigma_i^2} \left[y_i - \left\{ \sum_{k=1}^{K} B_k \exp\left[-\left(\frac{x_i - \mu_k}{\tau_k} \right)^2 \right] + \sum_{j=0}^{2} a_j x_i^j \right\} \right]^2. \quad (50)$$

As a practical matter, you might try $K = 2$ first and see if you obtain reasonable results. If not, try larger values of K. Of course this model introduces new nonlinear model parameters for each additional peak. The fitting of multiple overlapping peaks, with asymmetric peak models, to XPS spectra is considered in detail by Dunn and Dunn (1982).

Generally, the y_i are either gross counts C_i in channel i or, for background-subtracted spectra, net counts N_i in channel i. (Note that background subtraction removes only part of the generalized background, the B_n of Eq. (12).) If the $C(i)$ are gross counts, then one presumes that Poisson statistics apply and $\sigma^2(y_i)) \equiv \sigma_i^2 = C(i)$. If the spectrum is background-subtracted, then $\sigma^2(y_i) = C(i) + B_i$. If the $C(i)$ result from some other process, then one should use the appropriate variances in Eq. (50). For the nonlinear least-squares approach followed here, values of the model parameters $\mathbf{a}$ are chosen that minimize the merit function $\chi^2(\mathbf{a})$. To use the LM minimization method, partial derivatives of $\chi^2(\mathbf{a})$ with respect to each parameter are needed and for the above model are given by Eqs. (48).

An example of fitting two overlapping peaks is given in Example 3. In this example and in many nonlinear least-squares fitting analyses, the incremental path through the $\chi^2(\mathbf{a})$ hypersurface may often lead to physically unrealistic values of some of the parameters. This is particularly true for overlapping peaks. Unless one starts the minimizing search with very good guesses for the μ_k for each peak, often a broad positive Gaussian ($B_1 > 0$) with a negative Gaussian ($B_2 < 0$) results. Such is the case for Example 3. One way to avoid these unrealistic parameter values is to start the search very near the minimum of $\chi^2(\mathbf{a})$, which is seldom known a priori or to perform a *constrained* search along the hypersurface. In such a constrained search, the current values of the parameters are examined after each step, and if outside some preset range, an offending parameter is reset to the nearest range limit.

Example 3. Fit the model of Eq. (49) with $K = 2$ to the count data given in Table 2.

Solution 3. The LM method was used to find values of the best-fit parameters. The derivatives needed for this method are

$$\frac{dy(x|\mathbf{a})}{dB_i} = f(x, \mu_i, \tau_i), \quad i = 1, 2$$

Table 2 A portion of a spectrum giving channels and gross counts. The data points (x_i, y_i) to be fit are $x_i = i$ the channel number and $y_i = c(i)$ the counts in channel i

i	$C(i)$	i	$C(i)$	i	$C(i)$	i	$C(i)$
117	2210	127	4756	137	45,568	147	3827
118	2253	128	6176	138	36,698	148	3416
119	2333	129	9761	139	23,773	149	3156
120	2487	130	17,016	140	14,669	150	2896
121	2763	131	26,462	141	10,054	151	2713
122	2869	132	30,846	142	7666	152	2448
123	2984	133	28,392	143	6284	153	2335
124	3312	134	26,822	144	5387	154	2119
125	3629	135	32,667	145	4792	155	1957
126	4077	136	42,618	146	4224	156	1754

$$\frac{dy(x|\mathbf{a})}{d\mu_i} = Bf(x, \mu_i, \tau_i)\frac{2(x-\mu_i)}{\tau_i^2}, \quad i = 1, 2$$

$$\frac{dy(x|\mathbf{a})}{d\tau_i} = f(x, \mu_i, \tau_i)\frac{2(x-\mu_i)^2}{\tau_i^3}, \quad i = 1, 2 \qquad \frac{dy(x|\mathbf{a})}{da_j} = x^j, \quad j = 0, 1, 2. \tag{51}$$

The search for the minimum of $+\chi^2(\mathbf{a})$ began with the following dimensionless starting values:

$$\mu_1 = 130. \quad \sigma_1 = 2.200 \quad B_1 = 22,000. \quad \mu_1 = 140. \quad \sigma_2 = 2.800 \quad B_2 = 38,000.$$
$$a_0 = -177{,}000. \quad a_2 = 2680 \quad a_2 = -9.8400$$

After 15 steps, the initial value of $\chi^2(\mathbf{a})$ was reduced from 80,978. to 2034.92. Further iterations did not change $\chi^2(\mathbf{a})$. Values of the Best-fit parameters are

$$\mu_1 = 131.664 \pm 0.015 \qquad \sigma_1 = 2.1298 \pm 0.0157 \qquad B_1 = 23,403.4 \pm 137.7$$
$$\mu_2 = 136.734 \pm 0.0120 \qquad \sigma_2 = 2.8700 \pm 0.0138 \qquad B_2 = 38{,}538.5 \pm 129.0$$
$$a_0 = -166{,}321. \pm 1970. \qquad a_1 = 2517.03 \pm 29.22 \qquad a_2 = -9.2409 \pm 0.10771$$

The areas of the two Gaussians are

$$A_1 = \sqrt{\pi}\tau_1 B_1 = 88{,}348.1 \pm 552.78 \qquad A_2 = \sqrt{\pi}\tau_2 B_2 = 196{,}039. \pm 761.10$$

and the standard deviations of the peak are

$$\sigma_1 = \tau_1/\sqrt{2} = 1.5060 \pm 0.01108 \qquad \sigma_1 = \tau_1/\sqrt{2} = 2.0295 \pm 0.009724.$$

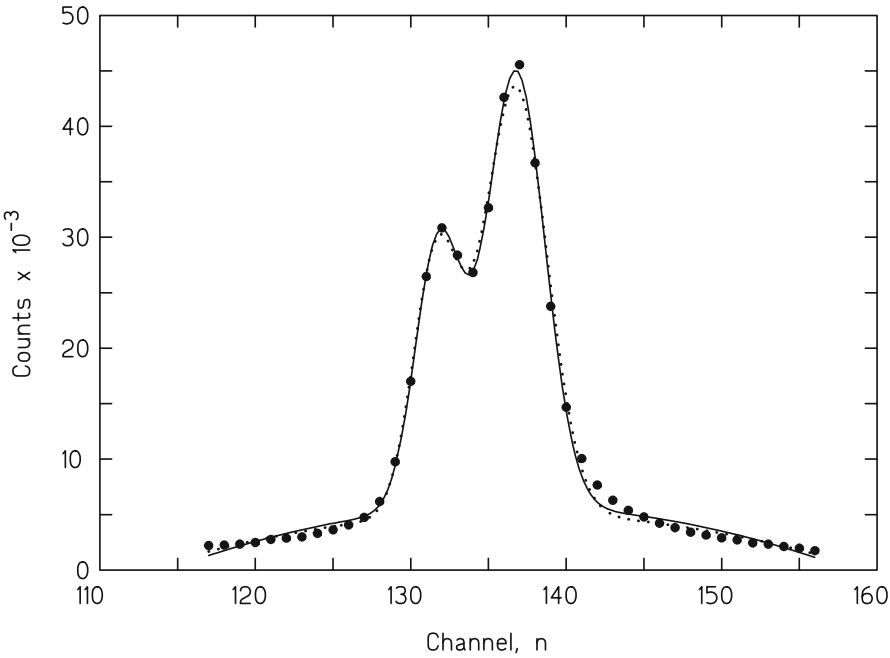

Fig. 9 A fit of two overlapping peaks with a quadratic background. The solid line is a weighted least-squares fit with $\sigma_i = \sqrt{c(i)}$, and the dotted line is an unweighted least-squares fit with $\sigma_i = 1$

The fit function is shown in Fig. 9.

It is seen that the model fits the data quite well. One would expect that a good model would be within the error intervals for about 68% of the data points, and this seems to be the case here. The uncertainty in each of the model parameters is small, relative to the parameter value, which also indicates a good fit. It is noted that the values of $i_1 = 117$ and $i_2 = 156$ are well beyond the 3σ range for the σ_1 and σ_2 obtained. Thus, the A_1 and A_2 values should be good estimates of the net areas under the two peaks.

Spectrum Stripping

If response functions can be collected or generated for all the sources (or radionuclides) that are expected to be present in an unknown sample and if the dependence of the response model is linearly related to the source strengths or radionuclide concentrations, then the method of spectrum stripping can be applied. This procedure is as follows:

- Collect a spectrum from the unknown sample.
- Identify the highest-energy peak in the spectrum.

- Subtract the response function for that energy peak, weighted by a constant, such that the peak is effectively removed.
- Proceed down the spectrum while subtracting other weighted response functions until all peaks are removed.

If the residuals are randomly distributed about zero or about some smooth background, then the specific response functions stripped from the spectrum for the unknown identify the radionuclides present, and the weighting constants estimate the source strength or concentration of each radionuclide.

Library Least-Squares

Because a detector produces a spectrum, even for a monoenergetic input, one can try to utilize the entire spectral response, or at least a significant part of it, rather than just the response values near each peak or set of overlapping peaks. The library least-squares approach, originally introduced by Marshall and Zumberge (1989), asks the following question: Why focus on only the peaks since other parts of the spectrum also contain information related to the abundances of the radionuclides that produce the peaks? One approach for using all of the information in a spectrum is the library least-squares (LLS) method, as implemented, for instance, by Gardner and Sood (2004) and Gardner and Xu (2009). The LLS method is based on a library that contains detector response functions for all radionuclides that might possibly be present in the sample whose spectrum is to be analyzed in order to determine the abundances of specific radionuclides. Then some fitting technique, such as least-squares or weighted least-squares, is used to fit the library spectra to the spectrum from a sample whose radionuclide abundances are sought.

This approach was not possible many years ago because one could not experimentally measure good spectra from all candidate radionuclides or a sufficient number of monoenergetic gamma rays. However, Monte Carlo modeling has become sufficiently robust that detector response functions can be calculated for almost any radionuclide. When Monte Carlo is used to generate detector response functions, the method often is referred to as Monte Carlo library least-squares (MCLLS). In this method, one calculates monoenergetic detector response functions $\mathcal{R}_n(E)$ for a wide range of discrete energies that can be emitted by sources of interest. Examples of such MC calculated detector response functions are shown in Fig. 10 and were calculated by special MC software and empirical resolution functions (Gardner and Sood 2004). The response function $\mathcal{R}_n(E)$ is the probability that a photon of energy E emitted by the source produces a count in channel n. This response function, as before, includes the probability a source photon reaches the detector, a probability which depends on the specific source-detector geometry, but it, generally, does not include photons scattered into the detector by material around the detector, i.e., the so-called roomshine.

To determine the concentrations of various radioisotopes present in a sample, response functions, per unit activity concentration, for each possible radioisotope

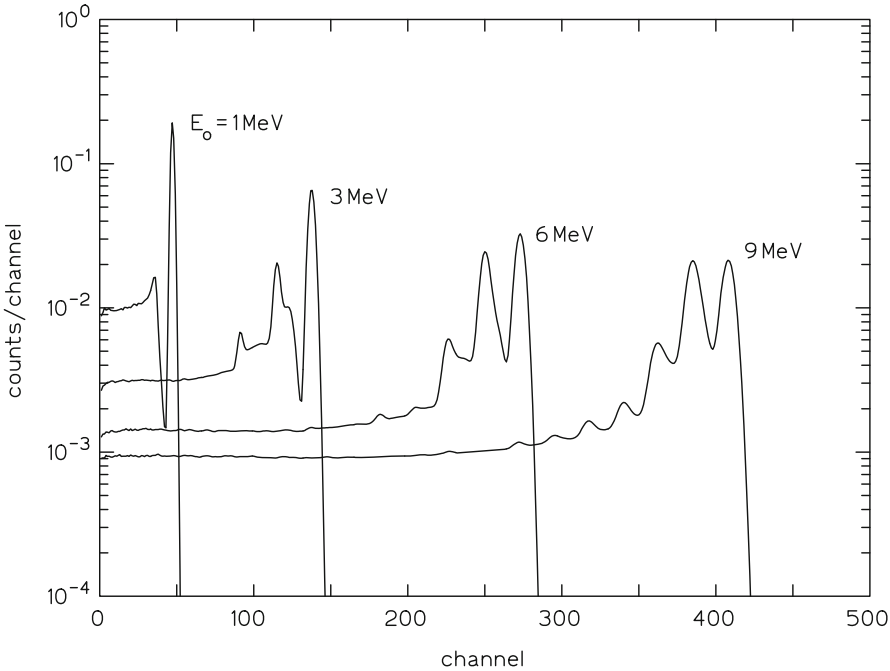

Fig. 10 Examples of library response functions $\mathcal{R}_n(E)$ for a 6 in × 6 in cylindrical NaI detector for monoenergetic photons normally and uniformly incident on the circular end of the crystal. No contribution from scattering in material around the detector is included as indicated by the absence of backscatter and annihilation peaks although several annihilation escape peaks from the crystal are evident. These response functions are a small part of the library for a 512-channel spectrum over the photon range 0–11.38 MeV. (Courtesy of Robin Gardner, NCSU)

likely to be in the sample must first be constructed. A library of such radioisotopic response functions $\mathcal{R}_n^k$ where $k = 1, 2, \ldots, K$ can be constructed from the monoenergetic response functions $\mathcal{R}_n(E)$, for a given source-detector geometry, as

$$\mathcal{R}_n^k = \sum_{i=1}^{I} f_i^k \mathcal{R}_n(E_i^k)\hat{\xi}^k, \tag{52}$$

where f_i^k is the frequency a photon of energy E_i^k, $i = 1, ..., I$ is emitted per decay of radionuclide k, and $\hat{\xi}^k$ is the decay rate of a unit activity concentration of the radionuclide.

Then the expected number of counts $y(n)$ recorded in channel n in a measurement time $\overline{T}$ produced by a sample of K possible radioisotopes is

$$y(n|\boldsymbol{\xi}) = T \sum_{k=1}^{K} \mathcal{R}_n^k \xi_k, \qquad n = 1, ..., N, \tag{53}$$

where ξ_k are the radioisotopic activity concentrations being sought. Again it is assumed all the activity concentrations remain constant over the measurement time $\overline{T}$. If $C(n)$ are the observed number of counts in channel n from the sample, then the vector $\boldsymbol{\xi}$, whose components are the concentrations ξ_k, can be determined as those values that minimize the merit function:

$$\chi^2(\boldsymbol{\xi}) = \sum_{n=1}^{N} W_n[c(n) - y(n, |\boldsymbol{\xi})]^2, \tag{54}$$

where W_n is a weight factor, often taken as $W_n = 1/\sigma^2(C(n)) = C(n)$. Because the response functions do not include background and roomshine, the counts $C(n)$ must first be corrected for these contributions. If a fitted ξ_k value is negative or near zero for one or more k, then the corresponding radionuclides might not be present in the sample. In this case, it is a good practice to remove the detector response functions for these radionuclides and repeat the analysis to see if a good fit is obtained.

The process just described assumes the response model is linear in the radionuclide concentrations and, thus, can be referred to as the *linear* LLS approach. This approach is very similar to the previous linear weighted least-squares process used to fit Gaussian distributions to spectral peaks. But here more features of the spectrum other than just the full-energy peaks are used. There are instances, however, in which the model is not linear in the radionuclide concentrations. Such cases arise in prompt gamma neutron activation analysis (PGNAA) and energy-dispersive x ray fluorescence spectroscopy (EDXRF).

Nonlinear Spectra

Generally, the samples used in a neutron activation analysis (NAA) are small, and their masses can be accurately measured, and because one is usually seeking concentrations of trace elements, an NAA analysis is well approximated as a linear process, and application of linear LS technique is appropriate. However, for bulk samples, a prompt gamma neutron activation analysis (PGNAA) is nonlinear, primarily for the following reasons:

- Sample mass, which often is not known, affects the flux density and the macroscopic capture cross section of the sample.
- The composition of the sample, which is unknown in advance, affects the spectrum. In particular, moisture content strongly affects the thermal-neutron flux density, which is what gives rise to the prompt gamma rays. Also, neutron absorbers affect the thermal flux density.

Thus, nonlinear models are needed for a PGNAA. Such models are iterative in nature and require the need to calculate spectral responses. Usually, Monte Carlo methods are used for such calculations. The general Monte Carlo library least-squares (MCLLS) approach in the nonlinear case proceeds as follows:

1. Assume values for the concentrations and use Monte Carlo to generate a complete spectrum for a sample of this assumed composition.
2. Keep track of the individual spectral responses for each element within the Monte Carlo code, so as to provide library spectra u_{nk} for each radionuclide.
3. Use linear LLS to estimate the radionuclide concentrations $\xi_k,\ k = 1, 2, \ldots, K$ from the sample spectrum.
4. If the calculated $\xi_k,\ k = 1, 2, \ldots, K$ match the assumed composition closely enough, you are done. If not, pick a new composition, based on the calculated concentrations, and repeat the process.
5. Iterate until you converge to the actual composition, to within a desired tolerance.

Results of this general procedure are given, for instance, by Gardner and Xu (2009).

Symbolic Monte Carlo

In x ray fluorescence, the responses are due to the *elements* present, but each element is composed of radionuclides, and the convention was introduced earlier to refer only to radionuclides. Hence, in the discussion below, elemental concentrations are called nuclide concentrations. Nonlinear matrix effects lead to absorption and enhancement in EDXRF. For instance, the characteristic x rays of nuclide a can be absorbed by elements with lower atomic numbers, which reduces the signal from nuclide a and enhances the signals for the lower atomic number nuclides. This effect means that the models in EDXRF also are not linear in the nuclide concentrations. Another implementation of Monte Carlo has been used in the EDXRF case. The method, originally called inverse Monte Carlo (IMC) (Dunn 1981), was applied to EDXRF by Yacout and Dunn (1987) for primary and secondary x rays. Mickael (1991) extended the work to include tertiary fluorescence.

The term IMC has been used for other purposes, e.g., to solve inverse problems by iterative Monte Carlo simulations in which the unknown parameters are varied until simulated and measured results agree sufficiently. The acronym IMC also has been used for "implicit Monte Carlo" (Gentile 2001). Thus, Dunn and Shultis (2009) recently proposed renaming the version of IMC that is non-iterative in the Monte Carlo simulations *symbolic Monte Carlo* (SMC) because the method proceeds by using symbols in the Monte Carlo scores for the unknown parameters.

SMC is a specialized technique in which the inverse problem of estimating the k and ξ_k is solved by a system of algebraic equations generated by a single Monte Carlo simulation. For purposes of illustration, a ternary system (one that contains three elemental nuclides) is considered. In essence, SMC creates models, with symbols for the unknown concentrations ξ_k, for the areas under all of the various x ray peaks (e.g., K_α and K_β) in a single simulation. The models depend on the detector efficiency as a function of energy; the nuclide concentrations; the primary, secondary, and tertiary fluorescence produced in the sample; and the background. For a ternary system, three equations result. The equations are rather complex (see Yacout and Dunn 1987 and Mickael 1991) but can be developed using only a single

Monte Carlo simulation. The advantage of this approach is that there is no need to iteratively run full Monte Carlo simulations as the assumed concentrations are varied. The disadvantage is that development of the model is involved and the algebraic equations are quite complex. Nevertheless, the method has been shown to work well in x ray spectroscopy and can, in principle, be applied to other spectroscopic applications, such as PGNAA, in which the responses are nonlinear functions of the concentrations.

Compton Suppression

Because prompt gamma rays tend to be of high energy (most are between 1 and 12 MeV), there is a large Compton component to the spectra, especially for thin semiconductor detectors. There are ways to reduce the Compton continuum. One is to partially surround a high-resolution germanium detector with scintillators, such as BGO, which has high efficiency because of its high density. The basic idea is that a photon that Compton scatters in the germanium detector has a reasonable chance of interacting in the scintillation crystals. These interactions occur at essentially the same time as the Compton scatter in the germanium and can thus be suppressed by an anticoincidence gate (the gate only accepts pulses in the germanium that are anticoincident with the scintillators). Fairly dramatic results can be achieved (Molnar 2004).

More About Spectroscopy Measurements

The purpose of radiation spectroscopy is to identify energetic emissions from radioactive materials. Such emissions are reported with several metrics, mainly the confidence in the identified energy or the *energy resolution* and the source activity (a function of the detector efficiency). The choice of detector is determined by the application and required spectroscopic performance. Detectors needed for field applications with sufficient spectroscopic performance to identify common isotopes may be best performed with lower-resolution scintillation detectors. Measurements requiring high-resolution spectroscopy generally require more expensive semiconductor spectrometers. No matter the type of spectrometer, it must undergo an energy calibration before any measurements can be made.

Channel Calibration

Calibration of the spectrometer channels in energy units is relatively simple, particularly if a linear energy/channel response is assumed. Typically two particle energies are chosen with relatively wide separation. For instance, ^{60}Co and ^{57}Co might be chosen. The peak channel $\tilde{n}_H$ for the higher-energy E_H and the peak channel $\tilde{n}_L$ for the lower-energy E_L are observed, and a simple linear fit between

these two channels provides a channel energy calibration, i.e.,

$$E(\tilde{n}) = \tilde{n}\left(\frac{E_H - E_L}{\tilde{n}_H - \tilde{n}_L}\right) + E_0, \tag{55}$$

where E_0 is the energy offset at channel $\tilde{n} = 0.0$, which is found from

$$E_0 = E_H - \tilde{n}_H\left(\frac{E_H - E_L}{\tilde{n}_H - \tilde{n}_L}\right). \tag{56}$$

For simplicity, the continuous $\tilde{n}$ is often taken as the channel number n which equals $\tilde{n}$ at the midpoint of a channel. The term in parentheses in the above equations is the energy width per channel ΔE and is an important spectrometer parameter because it defines the minimum energy resolution possible with the spectrometer.

Semiconductor materials usually show good signal linearity with energy deposition, but there are many scintillators that exhibit a nonlinear output with energy, especially at lower energies. Example scintillators include NaI(Tl) and CsI(Tl) in the energy region below 500 keV. For such nonlinear detectors, several energies in the nonlinear region should be used to fit a polynomial function to the channel energy calibration.

Spectroscopy Quality Metrics

Several quality metrics have been established, some official and others less so, that depend on the system and type of detector. These metrics are used to give the user an idea of the expected detector performance under different measurement conditions. Metrics include measurements of detection efficiency, energy resolution, channel width corrections, figure of merit, noise resolution, energy rate limit, and peak-to-Compton ratio. Many of these metrics are described in the IEEE Std 325–1996 document for HPGe detectors.

Detection Efficiency

There are multiple methods for defining and measuring the efficiency of a gamma-ray spectrometer. The efficiencies of most interest and utility are the absolute efficiency, the intrinsic efficiency, and the escape peak efficiency.

Total Intrinsic Detection Efficiency

The total intrinsic detection efficiency is defined by

$$\epsilon_{\mathrm{I}} = \sum_{i}^{N} \frac{A_{\mathrm{sp}}}{A\Omega_f t B_i}, \tag{57}$$

where A_{sp} are the recorded counts from the entire detector spectrum, t is the live time of the counts, A is the source activity, Ω_f is the fractional solid angle subtended by the detector, and B_i are the branching ratios of the radiation emissions. For instance, ^{60}Co emits two gamma rays per decay ($B = 2$), while only 85% of decays from ^{137}Cs result in the emission of a 661.7 keV gamma ray ($B = 0.85$). This metric ϵ_{I} yields some information about the overall detector counting efficiency, but does not give information on the energy resolution performance. Further, this particular metric is subject to changes with the LLD setting, and background contamination can skew the results.

Intrinsic Peak Efficiency

The intrinsic full-energy peak efficiency is defined by

$$\epsilon_{\mathrm{peak}} = \frac{A_p}{A\Omega_f Bt}, \tag{58}$$

where A_p are the recorded counts from the detector in the full-energy peak, t is the live time of the counts, A is the source activity, Ω_f is the fractional solid angle subtended by the detector, and B is the branching ratio of the emission under investigation. The intrinsic peak efficiency is similar to the intrinsic detection efficiency, except that A_p pertains only to those counts located in the background subtracted full-energy peak. It is notable that the intrinsic peak efficiency may be difficult to determine accurately for several detector types. For instance, the size and shape of an HPGe detector may be difficult to assess because the actual crystal is much smaller than the apparent cryogenic packaging. A similar situation exists with scintillation counters whose crystal is hermetically packed in a light-tight reflecting canister. The practical outcome of the intrinsic peak efficiency is a function of the packing canister, the absorbing material (NaI(Tl), HPGe, CdTe, etc.), the type of electrical contacts, the detector size, and the detector shape. Energy absorption in the detector encapsulation and contact dead layer affect the low-energy efficiency, while the atomic number and volume of the detector determine the high-energy efficiency. An example of the efficiency variation is shown in Fig. 11 for a 25% relative efficient, bulletized coaxial n-type HPGe detector (Kis et al. 1998).

A variety of gamma-ray sources can be used to measure the intrinsic peak efficiency over the energy region of interest. Afterward, a curve fit can be used as a predictive measure of efficiencies at other energies within the measured span (Kis et al. 1998). Although there are several curve-fitting functions offered in the literature, many examples listed in Kis et al. (1998), modern commercial curve-fitting computer programs are available that can provide high-fit r^2 values (>0.999).

Escape Peak Efficiency

The escape peak efficiency, mainly the single- and double-escape peaks from pair production, is a measure of the detector's ability to effectively recapture 511-keV annihilation photons. Larger escape peaks are indicative of larger losses. Although there are multiple definitions of this metric in the literature, a generally accepted

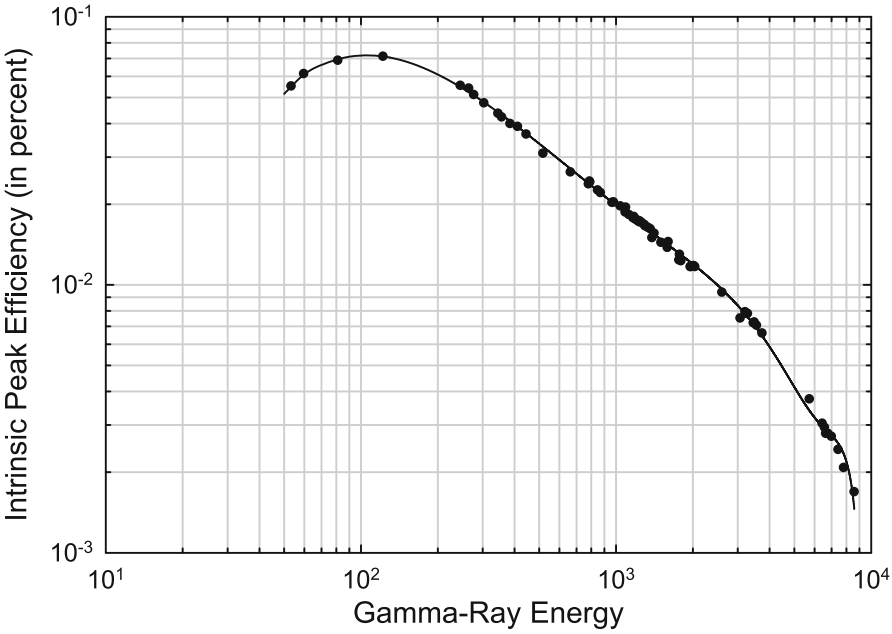

Fig. 11 Measured intrinsic peak efficiency for a 25% relative efficient n-type HPGe detector. The sources used for the calibration were ^{241}Am, ^{133}Ba, ^{152}Eu, ^{137}Cs, ^{60}Co, ^{188}Ta, ^{56}Co, ^{49}Ti, and ^{36}Cl. (Data acquired from Kis et al. 1998)

definition for the intrinsic escape peak efficiency is that described by Cline (1968) and Nafee (2011):

$$\epsilon_{es} = \frac{A_{\text{ep}}}{A\Omega_f Bt}, \tag{59}$$

where A_{ep} pertains to the number of counts in either the single-escape peak or the double-escape peak. To determine the number of counts in either escape peak, the subtraction method of Eq. (29) is employed. Equation 59 can be rewritten as

$$\epsilon_{es} = \epsilon_{\text{peak}} \frac{A_{\text{ep}}}{A_p}, \tag{60}$$

where the escape peak under investigation is for the corresponding full-energy peak.

It is notable that escape peaks can be used to identify the initial gamma-ray energies. Escape peaks do not have a Compton gap or Compton edge, and the apparent lack of these features can assist with their identification. Although gamma rays equal to or greater than 1.022 MeV can be absorbed through pair production, escape peaks usually do not become apparent for gamma-ray energies below approximately 1.5 MeV.

Energy Resolution

A method to determine the energy resolution of a gamma-ray spectrometer is prescribed by the IEEE Std 325–1996 and was developed for an HPGe detector and a ^{60}Co check source. The method makes no use of statistical uncertainties in the spectral count data (unlike the weighted least-squares fitting methods used earlier). Rather it depends on a very high number of counts in the full-energy peak so statistical uncertainties are of little consequence. The one unique feature of this standard, however, is that the method makes no Gaussian symmetry assumption about the shape of the full-energy peak and it is capable of treating asymmetric peaks that are wider at energies below the peak energy than above—a feature observed in many spectrometers. In essence, the method relies solely on manipulations of the observed channel counts $C(n) \equiv C_n$ to estimate the FWHM. McGregor and Shultis (2020) describe the analysis method with examples.

Perhaps, however, the most used method for determining energy resolution is to determine the FWHM of the energy peak under investigation directly from the data. This determination must be preceded by removing the background counts, as described earlier. When reporting the FWHM in terms of energy, the channel width is directly converted to energy (keV) using the channel energy calibration. When reporting the FWHM in terms of percent, the FWHM (whether in terms of energy or channels) is divided by the most probable energy (also in either energy or channel number) in that full-energy peak. Hence, the energy resolution in energy units and as a percent are

$$\mathrm{FWHM}_{\mathrm{energy}} = \Delta E \text{ keV} \quad \text{and} \quad \mathrm{FWHM}_{\%} = 100\frac{\Delta E}{E_\gamma}, \tag{61}$$

where ΔE is FWHM width in energy units (typically keV) and E_γ is the energy of the gamma ray. The usual standard for reporting energy resolution is to quote scintillator detector energy resolution in terms of percent and semiconductor detector energy resolution in terms of energy with units of keV. However, with many compound semiconductor detectors, there has been an unofficial departure from this standard, where many times the energy resolution is quoted in terms of percent.

Peak-to-Compton Ratio

Another metric specified for HPGe radiation spectrometers is the peak-to-Compton ratio (PCR). As described in the ANSI/IEEE standard 325–1996, the measurement of the PCR is performed with the 1332.5 keV gamma-ray energy from ^{60}Co. The PCR is defined as

$$\mathrm{PCR} = \frac{C_{\max}}{\overline{N}}, \tag{62}$$

where $C_{\max} = C_P$ is the number of counts in the peak channel for the 1332.5-keV gamma ray and $\overline{N}$ is the average number of counts per channel between the channels represented by 1040 and 1096 keV. The energy range between 1040 and 1096 keV

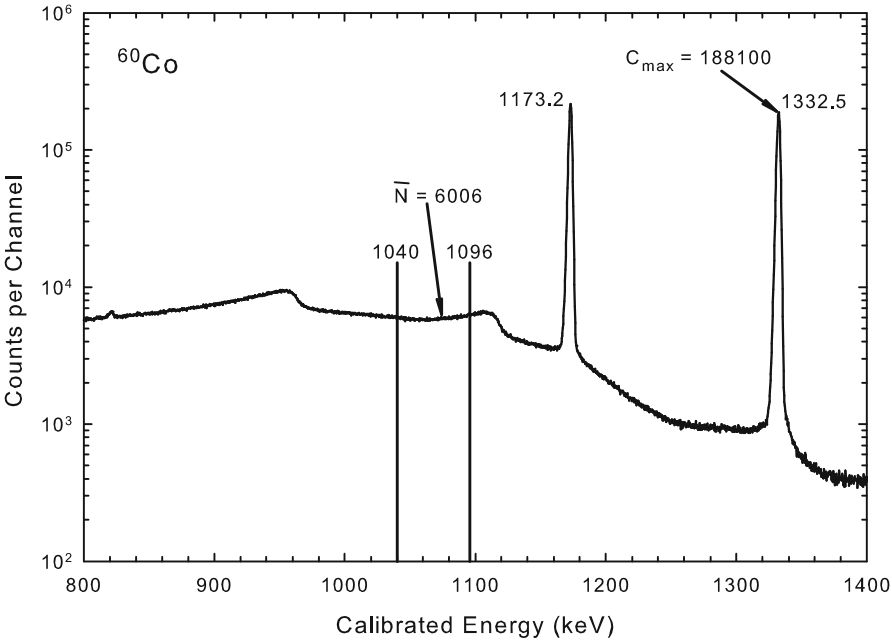

Fig. 12 The peak-to-Compton ratio (PCR) is calculated by dividing C_{max} by $\overline{N}$. In this example for a 20% relative efficiency HPGe coaxial detector, the measured PCR is 31.3. Copyright (2020). From Radiation Detection: Concepts, Methods and Devices by D.S. McGregor and J.K. Shultis. Reproduced by permission of Taylor and Francis Group, LLC, a division of Informa PLC

appears in the Compton gap of the 1173.2-keV gamma ray of ^{60}Co; therefore, it is almost entirely associated with the Compton continuum of the 1332.5-keV peak (see Fig. 12). The environmental background B should be subtracted from the measurements before calculating the PCR. The PCR metric is analogous to a sort of signal-to-noise ratio because the PCR is a measure of the spectrometer's ability to discern lower-energy and lower count rate gamma-ray peaks in the presence of higher-energy gamma-rays and their corresponding spectral features.

As the energy resolution of an HPGe detector improves, the number of counts in the 1332.5-keV peak channel increases. Also, as the size of the HPGe detector increases, so do counts in the 1332.5-keV peak channel because fewer scattered gamma rays can escape the detector. Hence, improved energy resolution and improved efficiency both tend to increase the PCR. PCR values can range from 30:1 for smaller HPGe detectors up to over 90:1 for relatively large detectors (Gilmore 2008).

It is notable that prior versions of the IEEE ANSI standard 325 also included a PCR for ^{137}Cs in which the maximum counts for the peak channel at 661.7 keV is divided by the average counts per channel in those channels between 358 and 382 keV. Although the ^{137}Cs-based PCR is generally not used to characterize HPGe detectors, it still has utility as a benchmark for comparing PCR values for

much smaller semiconductor spectrometers, such as those with CdZnTe or HgI_2 detectors whose peak efficiency at 1332.5 keV can be small compared to that of a HPGe detector. However, this particular definition does not appear in the most recent version ANSI 325–1996.

Peak-to-Valley Ratio

Another, less official, metric is the peak-to-valley ratio (PVR), which is measured with a ^{137}Cs source. This metric is defined as the number of counts in the peak channel divided by the number of counts in the middle of the Compton gap at 569 keV. This metric is seldom used for HPGe detectors; rather, it is more often used for compound semiconductor detectors and (rarely) used for experimental scintillation detectors. This metric provides a measure of the detector efficiency, energy resolution, and for semiconductors a measure of the charge carrier-trapping effects.

Peak-to-Total Ratio

The peak-to-total ratio (PTR) is the ratio of the total counts in a full-energy peak to the number of counts in the entire spectrum. The metric is useful with monoenergetic gamma-ray sources, such as ^{137}Cs and ^{54}Mn, but is not well defined or interpreted for polyenergetic gamma-ray sources. The peak-to-total ratio is proportional to the intrinsic full-energy peak efficiency ϵ_{peak} because

$$\epsilon_{\text{peak}} = \epsilon_{\text{I}} \left(\frac{\text{peak counts}}{\text{total counts}} \right) = \epsilon_{\text{I}} \text{PTR}, \tag{63}$$

where ϵ_{I} is the total intrinsic counting efficiency. By carefully selecting monoenergetic gamma-ray sources, the detector intrinsic peak efficiency can be calibrating over a broad energy range (Heath 1967). Unfortunately, there are a limited few practical monoenergetic gamma-ray sources to conduct such a measurement.

Another method to accomplish this same task is to use two detectors in coincidence, with the detector under investigation receiving the scattered gamma ray. The method entails capturing a Compton-scattered gamma ray that escapes from a high energy resolution primary (first) detector. The residual energy deposited in the second detector is determined by subtracting the energy deposited in the first detector from the known emission energy. Collimation and pulse-height discrimination can be used to select and allow only scattered gamma rays of a specific energy, thereby producing a pulse-height spectrum, at the energy under investigation, from the second detector.

Detectors for Gamma-Ray Spectroscopy

Typical methods of gamma-ray and x ray spectroscopy can be categorized as either energy-dispersive or wavelength-dispersive. Energy-dispersive spectroscopy (EDS) is perhaps the more popular technique, in which the energy of photons is preserved and recorded. Energy deposition indicators in the detector include light emission,

electrical current, and thermal changes. Wavelength-dispersive spectroscopy (WDS) is a technique in which a specific photon wavelength is measured by a witness detector. The witness detector position is translated in space so as to accumulate a spectrum of different photon wavelengths.

There are numerous detectors that can be used for radiation spectroscopy, which include versions of gas-filled, scintillation, and semiconductor detectors. However, only those commercial devices commonly used as analytical tools for gamma-ray and x ray spectroscopy are described in this chapter. EDS devices include scintillation, semiconducting, and cryogenic spectrometers. Diffractive spectrometers are classified as WDS devices and typically use gas-filled proportional counters as witness detectors.

Scintillation Spectrometers

Scintillators are generally separated into two classes: those being inorganic and organic. The method by which either produces scintillation light is physically different, hence the distinction. Inorganic scintillators can be found as crystalline, polycrystalline, or microcrystalline materials. Organic scintillators come in many forms, including crystalline materials, plastics, liquids, and even gases. However, organic scintillators, being composed of low Z materials, are ineffective as gamma-ray spectrometers and, thus, are not covered here.

The scintillation principle is quite simple. Radiation interactions occurring in a scintillator cause either atomic or molecular structure in the scintillator to become excited such that electrons are increased in energy. These excited electrons will de-excite, some of which will radiate light energy. The light emissions can then be detected with light-sensitive instrumentation.

A typical scintillation spectrometer consists of a scintillating material hermetically sealed in a reflecting canister. Typical canisters are cylindrical, with one end of the cylinder being an optically transparent window with all remaining surfaces being Lambertian reflectors. The optically transparent window is coupled to a light collection device, such as a photomultiplier tube (PMT), with an optical compound. The optical compound helps match the indices of refraction between the scintillation canister and the light collection device so as to reduce reflective losses. The PMT provides a voltage output that is linear with respect to the light emitted from the scintillator. Hence, the voltage "spectrum" is a linear indication of the radiation energy spectrum deposited in the detector. It is typical for commercial vendors to provide the scintillation canister and the PMT as one complete unit, although they can be acquired separately.

Inorganic Scintillators

Inorganic scintillators depend primarily on the crystalline energy band structure of the material for the scintillation mechanism. Shown in Fig. 13 is an energy band diagram for an inorganic scintillator. A lower-energy band, referred to as the valence energy band, has a reservoir of electrons. It is this band of electrons that participates in the binding of atoms. The next higher band is commonly referred to as the

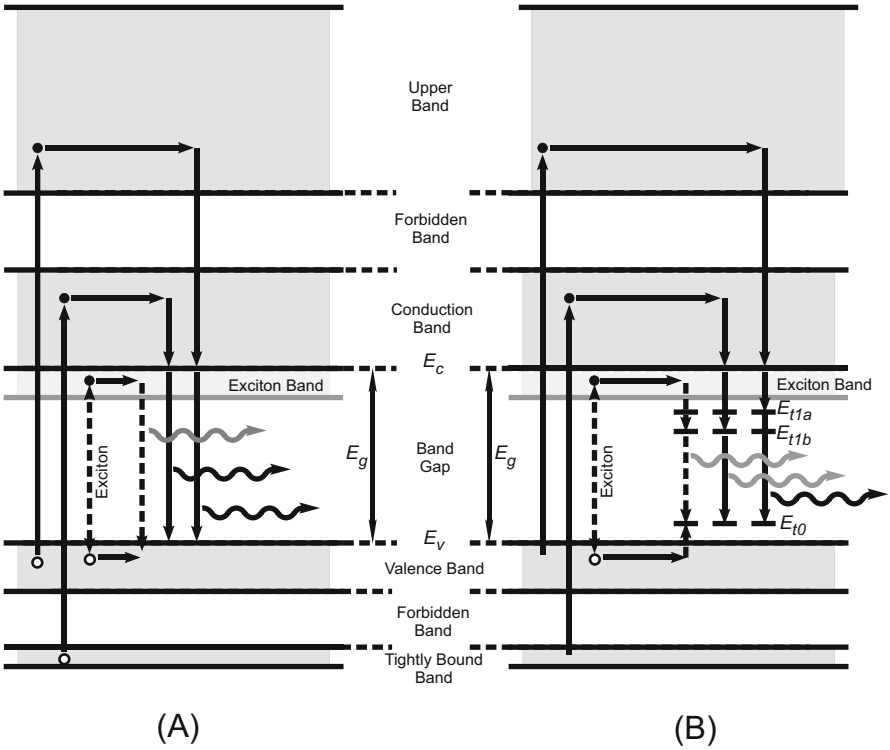

Fig. 13 Shown are two basic methods by which an inorganic scintillator produces light: (**a**) is the intrinsic case, and (**b**) is the extrinsic case. Copyright (2020). From Radiation Detection: Concepts, Methods and Devices by D.S. McGregor and J.K. Shultis. Reproduced by permission of Taylor and Francis Group, LLC, a division of Informa PLC

conduction band, which for inorganic scintillators is usually devoid of electrons. Between the two bands is a forbidden region where electrons are not allowed to exist, typically referred to as the energy band gap.

If a radioactive energy quantum, such as a gamma ray or charged particle, interacts in the scintillation material, it can excite numerous electrons from the valence band and the tightly bound bands up into the conduction bands (see Fig. 13a). These electrons rapidly lose energy and fall to the conduction band edge, E_C. As they de-excite and drop back into the valence band, they can lose energy through light emissions. Unfortunately, because the radiated energy of the photons is equivalent to the band gap energy, these same photons can be reabsorbed in the scintillator and again excite electrons into the conduction band. Hence, the scintillator can be opaque to its own light emissions. There are exceptions in which intrinsic scintillators work well. For example, bismuth germanate (BGO) releases light through optical transitions of Bi^{+3} ions, which release light that is lower in energy than the band gap and hence is relatively transparent to its own light emissions.

However, if an *impurity* or *dopant* is added to the crystal, it can produce allowed states in the band gap, as depicted in Fig. 13b. Such a scintillator is referred to as being *activated*. In the best of cases, the impurity atoms are uniformly distributed throughout the scintillator. When electrons are excited by a radiation event, they migrate through the crystal, many of which drop into the excited state of the impurity atom. Upon de-excitation, an electron will yield a photon equal in energy to the difference between the impurity atom excited and ground states. Hence, it will most likely not be reabsorbed by the scintillator material. Careful selection of the proper impurity *dopant* can allow for the light emission wavelength to be tailored specifically to match the sensitivity of the light collection device.

NaI(Tl) Scintillation Detectors

The most used inorganic scintillator current with the writing of this handbook is NaI(Tl), meaning that the scintillator is the salt NaI that has been activated with the dopant Tl. NaI(Tl) yields approximately 43,000 photons per MeV of energy absorbed in the crystal. Light is emitted from NaI(Tl) in a continuous spectrum, yet the most probable emission is at 415 nm, which matches well to typical commercial photomultiplier tubes. The decay time of NaI(Tl) is 230 ns, which refers to the time required to release 63.2% of the scintillation photons. It is the availability of large sizes and the acceptably linear response to gamma rays that make NaI(Tl) important. Many different sizes are available, ranging in size from cylinders that are only 0.5 inch diameter to almost a meter in diameter. Yet, the most preferred geometry remains the 3 × 3 inch (7.62 × 7.62 cm) right circular cylinder. It is the most characterized NaI(Tl) detector size with extensive efficiency data in the literature. Further, it is the standard by which all other inorganic scintillators are measured.

Because of its high efficiency for electromagnetic radiation (see Fig. 14), NaI(Tl) is widely used to measure x rays and gamma rays. x ray detectors with a thin entrance window containing a very thin NaI(Tl) detector are often used to measure the intensity and/or spectrum of low-energy electromagnetic radiation. NaI(Tl) detectors do not require cooling during operation and can be used in a great variety of applications. Compact spectrometers with NaI(Tl) coupled to an SiPM array are commercially available. The bare NaI(Tl) crystal is hygroscopic and fragile. However, when properly packaged, field applications are possible because they can operate over a long time period in warm and humid environments, resist a reasonable level of mechanical shock, and are resistant to radiation damage. Basically, for any application requiring a detector with a high gamma-ray efficiency and a modest energy resolution, the NaI(Tl) detector is clearly a good choice.

Other Inorganic Scintillation Detectors

Since the discovery of NaI(Tl) in 1948, the search has continued for a better scintillator for higher-energy resolution gamma-ray spectroscopy. There has been some limited success, which includes those scintillators listed in Table 3. For instance, CsI(Na) is similar in performance to NaI(Tl) but has a longer decay time. CsI(Tl) has much higher light output than NaI(Tl), but the emission spectrum

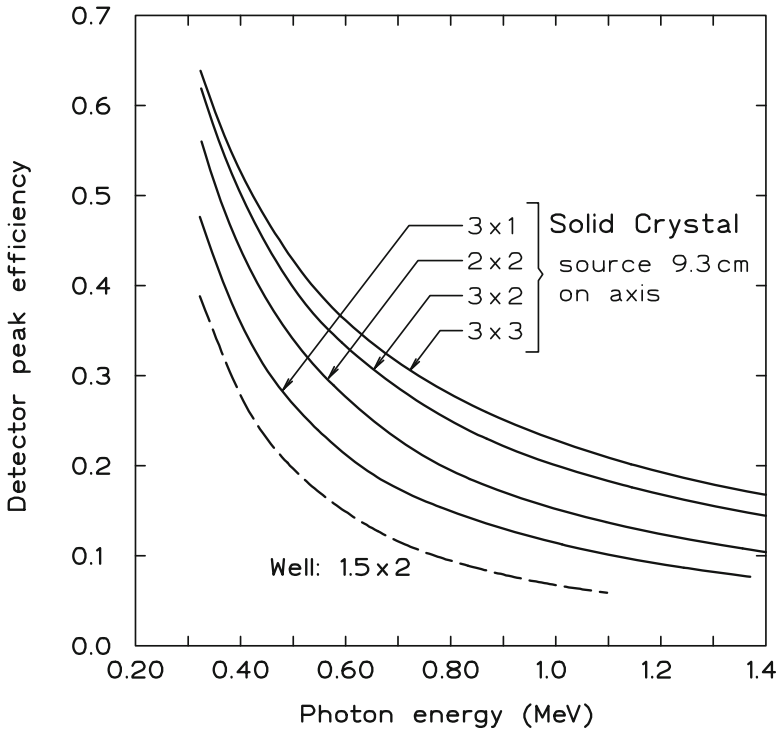

Fig. 14 Intrinsic peak efficiency for NaI(Tl) detectors

maximizes at 560 nm, which does not couple well to PMTs. However, CsI(Tl) has been coupled to Si photodiode sensors and silicon photomultipliers (SiPM) quite successfully. Bismuth germanate (BGO) has lower light output but is much denser and a better absorber of gamma rays. As a result, BGO is used for medical imaging systems, which helps to reduce the overall radiation dose that a patient receives during the imaging procedure. Over the past 10 years, lutetium oxyorthosilicate (LSO(Ce)), another heavy element scintillator, has become a popular alternative for medical imaging instrumentation, especially for PET scanning systems. LiI(Eu) is a scintillator that is primarily used for neutron detection, relying upon the ^{6}Li content in the crystal. In recent years, $LaBr_3$, a relatively new scintillator with exceptional properties for gamma-ray spectroscopy, has become available, demonstrating lower than 3% FWHM for 662- keV gamma rays. $LaBr_3$(Ce) has much higher light yield and a much shorter decay constant than NaI(Tl). Further, it is composed of higher Z elements and hence is a better gamma-ray absorber than NaI(Tl). However, it is extremely hygroscopic and fragile and hence is difficult to produce and handle. Although it has recently become commercially available, it is relatively expensive compared to NaI(Tl). A performance comparison between NaI(Tl), BGO, and $LaBr_3$(Ce) is shown in Fig. 15. Also, the various elpasolite scintillators have become

Table 3 Widely used inorganic scintillator materials with some of their properties

Scintillator	Density (g/cm^3)	Wavelength of maximum emission (nm)	Decay time (ns)	Light yield in photons/MeV	Relative PMT response compared to NaI(Tl)
NaI(Tl)	3.67	415	230	43,000	1.00
BGO	7.13	480	300	8200	0.13
CaF_2(Eu)	3.18	435	900	24,000	0.50
$CeBr_3$	5.2	371	17	68,000	ND
CsI(Na)	4.51	420	680, 3340	~45,000	1.10
CsI(Tl)	4.51	540	460, 4180	~57,500	0.49
CLYC(Ce)	3.31	372, 400	600, 6000	9565, 18,400	ND
CLLB(Ce)	4.2	420	180, 1100	43,000	1.15
CLLBC(Ce)	4.08	420	120, 500, 1500	45,000	~0.70
GSO(Ce)	6.71	440	56, 400	9000	0.20
$LaBr_3$(Ce)	5.29	380	16	63,000	1.30
$LaCl_3$(Ce)	3.86	350	28	49,000	0.70–0.90
LiI(Eu)	4.08	470	1400	15,000	0.23
LSO(Ce)	7.4	420	47	25,000	0.75
LuAP(Ce)	8.34	365	16.5, 74	11,400	ND
LuAG(Pr)	6.71	310	20–22	~18,000	ND
SrI_2(Eu)	4.55	435	1200	115,000	ND
YAP(Ce)	5.35	370	27	18,000	0.45
YAG(Ce)	4.55	550	88, 302	17,000	0.50

commercially available, the most common being CLYC(Ce), CLLB(Ce), and CLLBC(Ce). These elpasolite scintillations perform with good energy resolution and have added value as neutron detectors. Overall, there are numerous inorganic scintillators available for special radiation detection purposes. A review article on various inorganic scintillators can be found in the literature (McGregor 2018).

Light Collection

The light produced from a scintillation detector is collected by a photosensitive device, such as a photomultiplier tube, a photodiode, a microchannel plate, or a SiPM. The light is then converted to a measureable voltage pulse.

Photomultiplier Tubes

The photomultiplier tube (PMT) is commonly used to measure the light output from a scintillation detector. Referring to Fig. 16, the basic PMT has a photocathode which is located so as to absorb light emissions from a light source such as a scintillating material. When light photons strike the coating on the photocathode, they excite electrons which can diffuse to the surface facing the vacuum of the tube. A fraction of these excited electrons will escape the surface and leap into the vacuum tube. A voltage applied to the tube will guide the liberated electrons to an adjacent electrode named a dynode. As an electron approaches the dynode, it

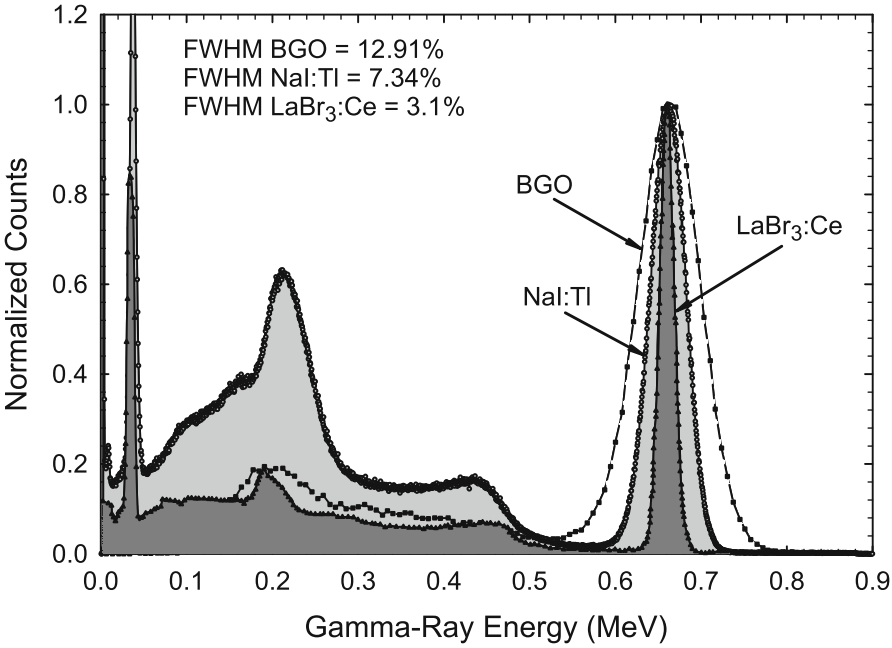

Fig. 15 Comparison of normalized spectral performance for a 2 × 2 NaI(Tl) detector, a 2 × 2 $LaBr_3$(Ce) detector, and a BGO detector of similar size. The source used was ^{137}Cs. Copyright (2020). From Radiation Detection: Concepts, Methods and Devices by D.S. McGregor and J.K. Shultis. Reproduced by permission of Taylor and Francis Group, LLC, a division of Informa PLC

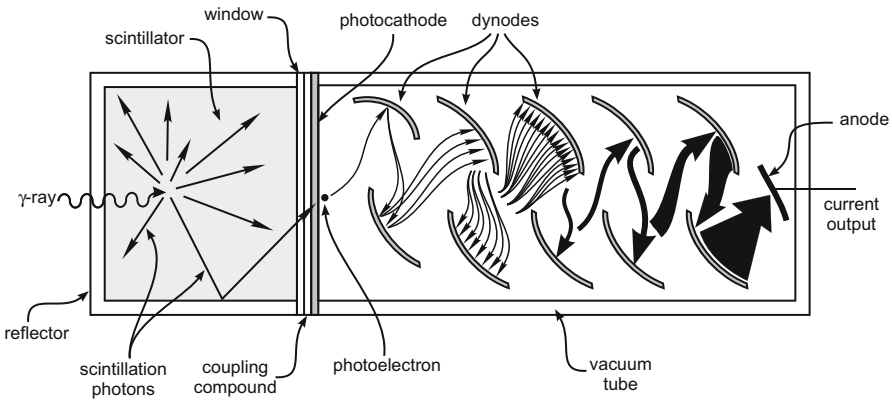

Fig. 16 The basic mechanism of a photomultiplier tube (PMT). An absorbed γ ray causes the emission of numerous light photons which can strike the photocathode. A scintillation photon that strikes the photocathode excites a photoelectron. The photoelectron is accelerated and guided to the first dynode with an electric field, where it strikes the dynode and ejects more electrons. These electrons are accelerated to the next dynode and excite more electrons. The process continues through the dynode chain until the cascade of electrons is collected at the anode, which is used to produce a voltage pulse (McGregor 2016)

gains velocity and energy from the applied voltage and electric field. Hence, when it strikes the dynode, it will again cause more electrons to become liberated into the tube. These newly liberated electrons are then guided to the next dynode where more electrons are liberated and so on. As a result, the total number of electrons released is a function of the number of dynodes in the PMT and the photoefficiency of the photocathode and the dynodes.

The total charge released in the PMT is

$$Q = qN_0G^n, \tag{64}$$

where q is the charge of an electron, N_0 is the initial number of electrons released at the photocathode, G is the number of electrons released per dynode per electron (the gain), and n is the total number of dynodes in the PMT. For instance, suppose that a PMT has 10 dynodes each operated with a gain of 4. An event that initially releases 1000 electrons (N_0) will cause over 10^9 electrons to emerge from the PMT.

The photomultiplier tube is an important tool in radiation detection, as it is the device that allowed scintillation materials to be used as practical detectors. It can take a minute amount of light produced in a scintillator from a single radiation absorption and turn it into a large electrical signal. It is this electrical signal, typically converted to a voltage pulse, that is measured from the scintillation detector system.

PMTs are stable and electronically quiet (low noise). Modern varieties have exceptional photocathode and dynode efficiencies, often referred to as quantum efficiency, with gains that can exceed 30. However there is a drawback. PMT materials used as photocathodes are generally fabricated from alkaline metals, which are most sensitive to light in the 350 to 450 nm range. Scintillators emitting light outside of these boundaries can still be used under some circumstances, yet their effectiveness can be severely compromised.

Microchannel Plates

Microchannel plates are an alternative method of amplifying signals from a scintillator. Microchannel plates are glass tubes with the insides coated with secondary electron-emissive materials. A voltage is applied across the tube length which causes electrons to cascade down the tube. Every time an electron strikes the tube wall, more electrons are emitted, much like with dynodes in a PMT. Hence, a single electron can cause a cascade that can eventually produce 10^6 electrons emitted from the other end of the tube. Typically, hundreds of these microchannels are bonded together to form a plate of channels running in parallel. The microchannel plate can be fastened to a common scintillator, whether organic or inorganic, which operates in a similar fashion as a PMT. Light photons entering the microchannel plate cause the ejection of primary photoelectrons, which cascade down the microchannels to liberate millions more electrons. The main advantage of a microchannel plate is its compact size, in which a microchannel plate only 1 inch thick can produce a signal of similar strength as a common PMT. The main problem with microchannel plates is the signal produced per monoenergetic radiation event is statistically much

noisier than that produced by a PMT; hence, the energy resolution for spectroscopy is typically worse than provided by a PMT.

Photodiodes

Photodiodes are actually semiconductor devices formed into a *pn* or *pin* junction diode. When photons strike the semiconductor, usually Si- or GaAs-based materials, electrons are excited. A voltage bias across the diode causes the electrons to drift across the device and induce charge much like a gas-filled ion chamber. The quantum efficiency of the semiconductor diode varies with device configuration and packaging. For instance, various different commercial Si photodiodes have peak efficiencies at wavelengths ranging between 700 and 1000 nm. Regardless, they are typically more sensitive to longer wavelengths than common commercial PMTs. As a result, CsI(Tl) emissions match better to Si photodiodes than PMTs. Photodiodes operate with low voltage; are small, rugged, and relatively inexpensive; and hence offer a compact method of sensing light emissions from scintillators. However, they typically do not couple well to light emissions near the 400 nm range (blue-green) and have low gain, if any at all. Consequently, the signals from photodiodes need more amplification than signals from PMTs, and scintillator/photodiode systems generally produce worse energy resolution than do scintillator/PMT systems.

Silicon Photomultipliers

Junction breakdown of semiconductors can be used as another means of radiation counting and spectroscopy. For any *pn* junction operated with a reverse bias voltage, there is a voltage above which the junction "breaks down" and continues to conduct current across the semiconductor. This phenomenon is initiated by three different means, namely (1) thermal instabilities, (2) tunneling current, and (3) avalanche breakdown. The avalanche process is solely dependent upon what occurs within the diode depletion region W_d. Hence, an event that excites a charge carrier within the active depletion region may trigger an enormous, continuous avalanche from impact ionization with gains exceeding 10^6. This interesting mode of operation is usually not preferred for avalanche photodiode operation (APD) operation, the effects of which were studied by McIntyre (1961) and Haitz (1961).

However, there are particular applications in which the breakdown mode of operation is beneficial, mainly realized with the single-photon avalanche diode (SPAD), so-named because of its ability to detect low light levels, one photon at a time. The leading edge of an avalanche signal marks the arrival time of the interacting photon within the depletion region. After the avalanche is triggered, the self-sustained current continues to flow unless quenched. Often a series resistance is included in the design that serves to quench the avalanche, much like an externally quenched GM counter. As a matter of fact, APDs designed and operated in this mode are often said to operate in "Geiger mode" (Renker 2006). As the avalanche current flows through the quenching resistance, it draws voltage from the source, thereby causing the voltage across the APD to drop below the breakdown voltage, causing the avalanche to cease. As a result, the output current and collected charge are nearly the same for each avalanche regardless of energy deposition in the device, statistical

fluctuations notwithstanding. Consequently, if two or more photons interact in the device simultaneously, the total charge liberated from the quenched avalanche is roughly the same as if a single photon caused the avalanche, again much like a GM counter.

Silicon photomultipliers (SiPM) use the breakdown condition with thousands of tiny silicon APDs arranged into a compact array, presently on the order of 6×6 mm area or less. The individual APDs in silicon photomultipliers (SiPM) have linear dimensions usually between 20 and 100 μm; a common size is 35×35 μm per APD pixel. Hence, a single SiPM array may have more than 10^4 APD pixels. Each APD is electrically decoupled from adjacent APDs with polysilicon resistors fabricated on the same substrate. Typical operational bias voltage is 10% to 15% above the breakdown voltage.

SiPMs are commercially available and in some applications are replacing the traditional PMT. A scintillator may be fastened to the SiPM face, much like a conventional PMT, and light from radiation interactions within the scintillator triggers the APDs. Each APD provides information that is ultimately limited to recognizing the excitation of an initial electron-hole pair within the avalanche region. Because each pixel produces an avalanche of relatively the same magnitude per event, the total photon count can be determined by dividing the total measured charge by the avalanche gain. Hence, the device operates mainly as a photon counter, and the total measured current is proportional to the total number of photons. The enormous gain per pixel, when the pixel counts are added together, can produce more than 10^9 free electrons per event.

A particular advantage of SiPMs is the high quantum efficiency of Si for photons with wavelengths between 350 and 950 nm. The photon detection efficiency of an SiPM can be much higher than a common PMT. However, many commercial SiPM units are designed with peak sensitivity near 420 nm, similar to conventional bialkali PMTs. SiPMs are compact and rugged, perhaps one of the most useful features of SiPMs. They need only modest power, usually requiring no more than a few tens of volts for operation. SiPMs are also insensitive to magnetic fields, thereby making them an attractive choice for applications in areas where high magnetic fields may arise.

Factors Affecting Energy Resolution

The energy resolution achievable from a scintillation spectrometer is determined by a number of factors, including brightness, reflector efficiency, light collection efficiency, PMT quantum efficiency, activator uniformity, and scintillator light yield linearity. Simplistically, the energy resolution can be described as

$$\mathcal{R}^2 = R_s^2 + R_p^2, \tag{65}$$

where R_s is the energy resolution contribution relating to the scintillation crystal and encapsulation and R_p is the energy resolution contribution relating to the photon detection device. The term R_s can be described by

$$R_s^2 = R_n^2 + R_i^2 + R_t^2 + R_d^2, \tag{66}$$

where R_n is resolution broadening from statistical fluctuations in the number of electrons excited by monoenergetic absorption events, R_t is resolution broadening from variations in light transfer to the light detection device, R_i is resolution broadening from inhomogeneity, and R_d is the nonproportionality of response. The variance R_n^2 can be expected to follow a somewhat Gaussian distribution, corrected with the appropriate Fano factor to correct energy band structure. The distribution of dopants in the scintillator may not be homogeneously distributed in the material, causing spatially dependent variations R_i^2 in the number of electrons diffusing to the photon-producing activator sites. Although reflectors around scintillator detectors can be quite efficient, the angle at which photons strike the light collector (PMT, for instance) may cause variations R_t^2 in the number of photons that actually enter the light detector. Other factors affecting the light transfer variation include nonuniform clarity of the scintillator, imperfections in the reflector, and nonuniformity of the coupling compound between the scintillator and the light detection device. Most scintillators have a nonlinear light yield as a function of absorbed photon energy, which is especially true in the energy range between a few keV up to 1 MeV. As a result, there will be a variation R_d^2 in the number of photons produced for monoenergetic gamma rays, depending on if the photon was absorbed through a single photoelectric event or numerous Compton scatters.

The light collection terminates at the photodetection device, typically a PMT or SiPM, in which the light is converted into an electron signal. The conversion efficiency and variance R_p^2 of the light collection efficiency are affected by the wavelength of light striking the device and uniformity of the collecting layers. For instance, scintillators emit a spectrum of photon wavelengths, which may or may not match well to the quantum conversion efficiency of the PMT photocathode or the SiPM material. Further, the photocathode layer will have some amount of variance in thickness, which affects the variance in the number of electrons ejected from the photocathode per initial gamma-ray interaction event. With SiPMs, it is possible that two or more photons simultaneously strike the same pixel, resulting in only one of the photons being recorded. As the photon flux increases (brighter scintillator or higher gamma-ray energy), this effect increases, and more scintillation photons are not recorded, causing nonlinearity in the pulse-height spectrum.

Semiconductor Spectrometers

In some way, the operation of a semiconductor detector combines the concepts of the charge excitation method in a crystalline inorganic scintillator and the charge collection method of a gas-filled ion chamber. Referring to Fig. 17, gamma rays or charged particles that are absorbed in the semiconductor will excite electrons from the valence and tightly bound energy bands up into the numerous conduction bands. The empty states left behind by the negative electrons will behave as positively

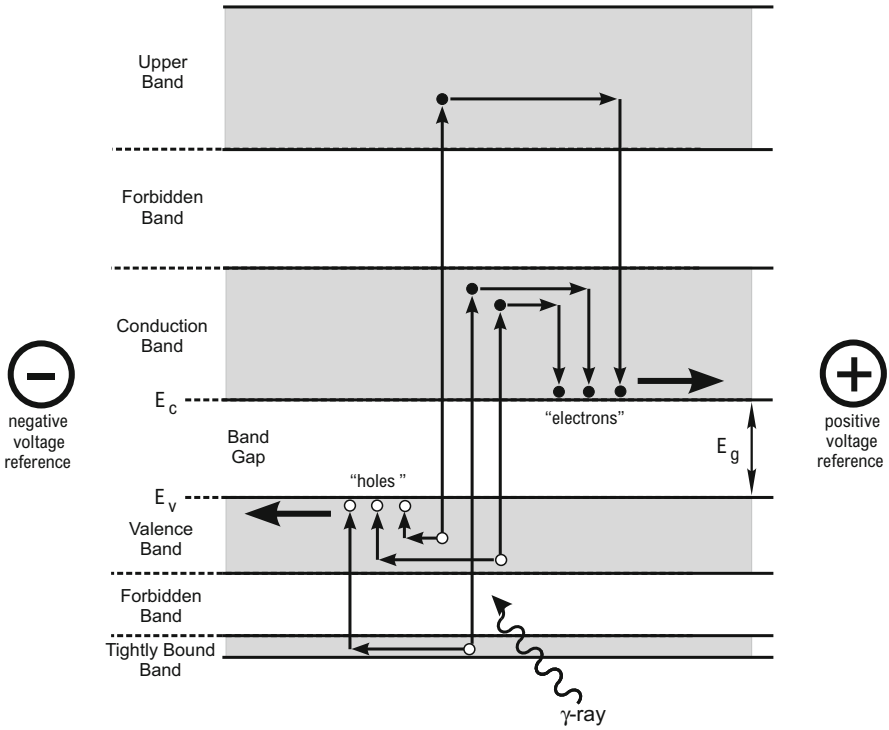

Fig. 17 Absorbed radiation energy excites electrons from the valence and tightly bound bands up into the higher conduction bands, in a similar manner as excitation occurs in a crystalline inorganic scintillator. The empty states left behind, referred to as *holes*, behave as positive charges. The electrons quickly de-excite to the lowest conduction band edge, E_C, and the holes rapidly de-excite to the top of the valence band, E_V. A voltage applied to the detector causes the electron and hole charge carriers to drift to the device contacts, much in the same manner as electron-ion pairs drift to the electrical terminals in a gas-filled ion chamber (McGregor 2016)

charged particles generally referred to as *holes*. The excited electrons will rapidly de-excite to the conduction band edge, E_C. Likewise, as electrons high in the valence band fall to lower empty states in the valence and tightly bound bands, it gives the effect of holes moving up to the valence band edge, E_V.

A single major difference between a semiconductor and almost all scintillators is that the mobility of charge carriers in semiconductors is high enough to allow for conduction, whereas scintillation materials are mostly insulating materials that do not conduct. As a result, a voltage can be applied across a semiconductor material that will cause the negative electrons and positive holes, commonly referred to as *electron-hole pairs*, to drift in opposite directions, much like the electron-ion pairs in a gas-filled ion chamber. In fact, at one time semiconductor detectors were referred to as "solid-state ion chambers." As these charges drift across the semiconductor,

Table 4 Common semiconductors and properties

Semiconductor	Atomic numbers (Z)	Density ($g\,cm^{-3}$)	Band gap (eV)	Ionization energy (eV per e-h pair)	Fano factor
Si	14	2.33	1.12	3.61	≈0.10
SiC(4H)	14/6	3.21	3.23	7.8	–
Ge	32	5.33	0.72	2.98	≈0.08
GaAs	31/33	5.32	1.42	4.2	≈0.18
CdTe	48/52	6.06	1.52	4.43	≈0.15
$Cd_{0.8}Zn_{0.2}Te$	48/30/52	6.0	1.60	5.0	≈0.09
HgI_2	80/53	6.4	2.13	4.3	≈0.19

they induce a current to flow in an external circuit which can be measured as a current or stored across a capacitor to form a voltage.

Semiconductors are far more desirable for energy spectroscopy than gas-filled detectors or scintillation detectors because they are capable of much higher-energy resolution. The observed improvement is largely due to the better statistics regarding the number of charges produced by a radiation interaction. Typically, it only takes 3–5 eV to produce an electron-hole pair in a semiconductor (Table 4). By comparison, it takes between 25 and 40 eV to produce an electron-ion pair in a gas-filled detector and between 100 eV to 1 keV to produce a single photoelectron ejection from the PMT photocathode in a scintillation/PMT detector (primarily due to light reflections and poor quantum efficiency at the photocathode). Hence, statistically, semiconductors produce more charge carriers from the primary ionization event, which determines the statistical fluctuation in the energy resolution.

Most semiconductor detectors are configured as either planar or coaxial geometries, as shown in Fig. 18. Small semiconductor detectors are configured as planar devices and can be used for charged particle detection and gamma-ray detection. Large semiconductor gamma-ray spectrometers are often configured in a coaxial form to reduce the capacitance of the detector (which can affect the overall energy resolution). There are three basic methods generally used to reduce leakage currents through semiconductor detectors. Most commonly the semiconductors are formed into reverse biased *pn* or *pin* junction diodes, which are the case for Ge, Si, GaAs, and InP detectors. Alternatively, highly resistive semiconductors, such as CdTe, CdZnTe, and HgI_2, need only to have ohmic contacts since the bulk resistance of the material is high enough to effectively reduce leakage currents. Finally, large detectors, such as high-purity Ge detectors and lithium-drifted Si detectors, are chilled with liquid nitrogen (LN2) or a mechanical refrigerator to reduce thermally generated leakage currents.

Ge Detectors

Although Li drifting allowed Ge-based semiconductor gamma-ray spectrometers, denoted Ge(Li)detectors, to be realized, it came with problems. Li is highly mobile

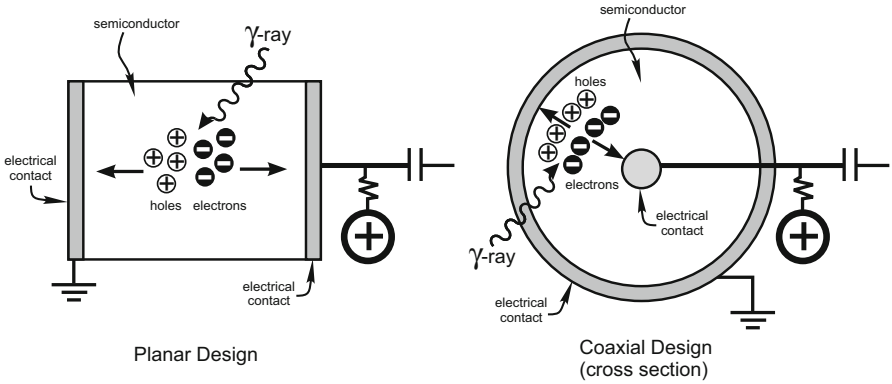

Fig. 18 The most common designs for semiconductor detectors are the planar and coaxial configurations (McGregor 2016)

in Ge and must be locked into place by immediately freezing the Ge crystal with LN2 after the drifting process is finished. Further, if Ge(Li) detectors were ever allowed to warm up, the Li would diffuse and redistribute, hence ruining the detectors. As a result, Ge(Li) detectors had to constantly be kept at LN2 temperatures, a major inconvenience. Zone refinement of Ge materials now allows for impurities to be removed from the material such that Li drifting is no longer necessary. Hence, Ge(Li) detectors have been replaced by high-purity Ge detectors, denoted HPGe detectors. However, HPGe detectors must still be chilled with LN2 *when operated* in order to reduce excessive thermally generated leakage currents.

HPGe detectors have exceptional energy resolution compared to scintillation and gas-filled detectors. The dramatic difference in the energy resolution between NaI(Tl) and HPGe spectrometers is shown in Fig. 19, where there is a spectroscopic comparison of measurements made of a mixed ^{152}Eu, ^{154}Eu, and ^{155}Eu radiation source. HPGe detectors are standard high-resolution spectroscopy devices used in the laboratory. Their high-energy resolution allows them to easily identify radioactive isotopes for a variety of applications, which includes impurity analysis, composition analysis, and medical isotope characterization. Portable devices with small LN2 dewars are also available for remote spectroscopy measurements, although the dewar capacity allows for only 1 day of operation. Hence, a source of LN2 must be nearby for such an apparatus. Much improvement has been realized with small mechanical refrigerators, and commercial HPGe detectors with portable refrigerator units are available, thereby largely mitigating the need for an LN2 source.

The gamma-ray absorption efficiency for Ge ($Z = 32$) is much less than that for the iodine ($Z = 53$) in NaI(Tl). Due to the higher atomic number and generally larger size, NaI(Tl) detectors often have higher detection efficiency for high-energy gamma rays than do HPGe detectors (but much poorer energy resolution). When first introduced, Ge detector efficiency was commonly compared to that of a

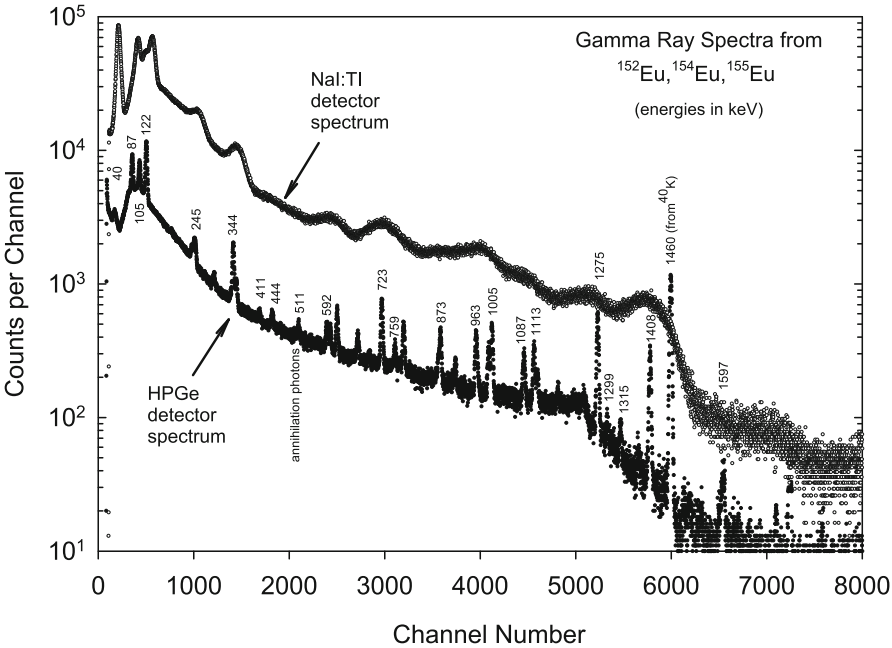

Fig. 19 Comparison of the energy resolution between a NaI(Tl) and an HPGe detector. The gamma-ray source is a mixture of ^{152}Eu, ^{154}Eu, and ^{155}Eu [McGregor 2008]

3-inch-diameter × 3-inch-long (3×3) right circular cylinder of NaI(Tl) for 1332 keV gamma rays from ^{60}Co. Even today, the *relative* efficiency of a Ge detector is quoted in terms of a 3 × 3 NaI(Tl) detector. For instance, a 60% efficient HPGe detector will have 60% of the efficiency that a 3 × 3 NaI(Tl) detector would for 1332 keV gamma rays from ^{60}Co. HPGe detectors are much more expensive than NaI(Tl) detectors and hence are best used when gamma-ray energy resolution is most important for measurements. If efficiency is of greatest concern, it is often wiser to use a NaI(Tl) detector. Still, although expensive, modern manufacturers do produce larger HPGe detectors with 200% efficiency (as compared to a 3 × 3 NaI(Tl) detector).

Si Detectors

The problem with Li redistribution does not apply to Si, hence Si(Li) detectors are still manufactured and available. Since Si(Li) detectors have a much lower atomic number than HPGe, their relative efficiency per unit thickness is significantly lower for electromagnetic radiation. However, for x ray or gamma-ray energies less than about 30 keV, commercially available Si(Li) detectors are thick enough to provide performance which is comparable to HPGe detectors. For example, a 3–5 -mm-thick detector with a thin entrance window has an efficiency of 100% near 10 keV. Si(Li) detectors are preferred over HPGe detectors for low-energy x ray measurements, primarily due to the lower-energy x ray escape peak features that appear in a Si(Li)

detector spectrum as opposed to an HPGe detector spectrum. Further, background gamma rays tend to interact more strongly with HPGe detectors than with Si(Li) detectors, which also complicates the x ray spectrum. Based upon the fact that a majority of the applications require a thin window, Si(Li) detectors are often manufactured with thin beryllium windows. Typically, Si(Li) detectors are chilled with LN2 to reduce thermal leakage currents, improving performance.

High-purity Si detectors, which do not incorporate Li drifting, are also available but are significantly smaller than HPGe and Si(Li) detectors. Such devices are typically only a few hundred microns thick and are designed for charged-particle spectroscopy. They range in diameter from one cm to several cm. The detectors are formed as diodes to reduce leakage currents and use either a thin metal contact or a thin implanted dopant layer contact to produce the rectifying diode configuration. The devices are always operated in reverse bias to reduce leakage currents. Heavy charged particles, such as alpha particles, rapidly lose energy as they pass through a substance, including the detector contacts. In order to preserve the original energy of charged particles under investigation, the detector contacts and implanted junctions are relatively thin, typically being only a few hundred nanometers thick to reduce energy loss in the contact layer. Further, the measurements are typically conducted in a vacuum chamber to reduce energy loss otherwise encountered by the alpha particles in air. Since the detectors are not very thick, they do not have much thermal charge carrier generation and consequently do not need to be cooled during operation.

Compound Semiconductor Detectors

Although HPGe and Si(Li) detectors have proven to be useful and important semiconductor detectors, the fact that they must be chilled with either LN2 or a refrigerator is a considerable inconvenience. Hence, much research has been devoted to the search for semiconductors that can be used at room temperature. The main requirement is that the band gap energy (E_g) be greater than 1.4 eV, which seriously limits the field of candidates. Further, the material must be composed of high atomic numbers for adequate gamma-ray absorption. As a result, there are only a few candidates, all of which are compound semiconductors, meaning that they are composed of two or more elements. Hence, the issues regarding crystal growth defects and impurities become far more problematic. Still, there are several materials that show promise, three of which are briefly mentioned here.

HgI_2, CdTe, and CdZnTe Detectors

Mercuric iodide (HgI_2) has been studied since the early 1970s as a candidate gamma-ray spectrometer and has been used for commercial x ray spectrometry analysis tools. The high atomic numbers of Hg ($Z = 80$) and iodine ($Z = 53$) make it attractive as an efficient gamma-ray absorber, and its large band gap of 2.13 eV allows it to be used as a room temperature gamma-ray spectrometer. However, the bright red crystals are difficult to grow and manufacture into detectors. The voltage required to operate the devices is excessive, usually 1000 volts or more for a device

only a few mm thick. HgI_2 detectors degrade over time, an effect referred to as polarization, which is another reason why they do not enjoy widespread use.

Cadmium telluride (CdTe) has been studied since the late 1960s as a candidate gamma-ray spectrometer. They have relatively good gamma-ray absorption efficiency, with Cd ($Z = 48$) and Te ($Z = 52$). The band gap of 1.52 eV allows CdTe to be operated at room temperature. Compared to HgI_2, the crystals are easier to grow and are not as fragile. Further, although still difficult to manufacture, detectors are easier to produce than HgI_2. There are commercial vendors of CdTe detectors, although the devices are relatively small, typically being only a few mm thick with area of only a few mm^2. CdTe detectors have been used for room temperature-operated low-energy gamma-ray spectroscopy systems and also for electronic personal dosimeters. Over time, CdTe detectors also suffer from polarization.

Cadmium zinc telluride (CdZnTe or CZT) has been studied as a gamma-ray spectrometer since 1990. By far, the most studied version of CZT has 10% Zn, 40% Cd, and 50% Te molar concentrations, which yields a band gap energy of approximately 1.6 eV. CZT detectors offer an excellent option for low-energy x ray spectroscopy where cooling is not possible. Although the detectors are quite small compared to HPGe and Si(Li) detectors, they are manufactured in sizes ranging from 0.1 to 2.5 cm^3, depending on the detector configuration. Still, due to their small size, they perform best at gamma-ray energies below 1.0 MeV. Various clever electrode designs have been incorporated into new CZT detectors to improve their energy resolution, and CZT has become the most used compound semiconductor for gamma-ray spectroscopy. Some detector cooling (near −30 °C), usually performed with miniature electronic Peltier coolers, improves the resolution performance, although excellent performance can be achieved at room temperature. The average ionization energy is 5.0 eV per electron-hole pair, which is greater than Ge (2.98 eV) or Si (3.6 eV). Hence, the resolution of CZT detectors is not as good as HPGe or Si(Li) detectors, although much better than gas-filled and scintillation detectors (Fig. 20). When LN2 chilling is not an option, CZT detectors are a good choice for radiation measurement applications requiring good energy resolution. Typically, CZT detectors do not show polarization effects.

Factors Affecting Energy Resolution

The energy resolution achievable from a semiconductor spectrometer is largely determined by the average ionization energy, leakage currents, electronic noise, mean free drift times, and the charge carrier mobilities. Energy resolution is quoted in terms of energy spread at the full width at half the maximum (FWHM) of a spectral full-energy peak,

$$\mathrm{FWHM} = \left[(\mathrm{FWHM}_{noise})^2 + \left(2.35\sqrt{wFE}\right)^2 \right]^{1/2}, \tag{67}$$

where w is the average energy to produce an electron-hole pair, E is the photon energy, and F is the Fano factor (typically 0.1). The Fano factor is a correction

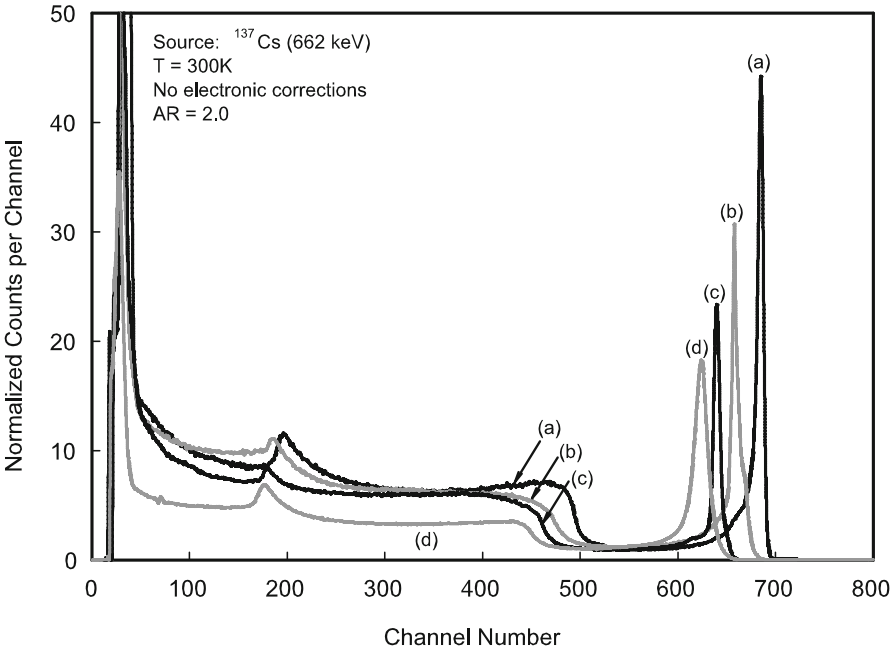

Fig. 20 Spectroscopic results from ^{137}Cs for several Frisch collar CdZnTe detectors, each having a 2:1 aspect ratio. The sizes and FWHM resolutions are (**a**) 0.9% for a 4.7 × 4.7 × 9.5 mm device, (**b**) 1.1% for a 6.5 × 6.5 × 13 mm device, (**c**) 1.2% for a 7.8 × 7.8 × 15.6 mm device, and (**d**) 2.4% for a 11 × 11 × 22 mm device. (After Kargar et al. 2009)

factor to account for typically higher-energy resolution than predicted from pure Gaussian statistics. For semiconductor detectors with short charge carrier mean free drift times $\tau_{e,h}$ and low charge carrier mobilities $\mu_{e,h}$, the energy resolution will suffer from loss of charge carriers during the collection process. Consequently there is a variance in the current measured from monoenergetic gamma-ray events as a function of the interaction position and detector size.

The total charge collected is usually affected by crystalline imperfections that serve as *trapping* sites, which are energy states that remove free charge carriers from the conduction and valence bands. Charge is induced while these charge carriers are in motion; hence, their removal diminishes the output voltage. Although the actual trapping process is complicated, it is typical to describe the relative charge collection efficiency as a simplified function of trapping. For planar-shaped detectors, the induced charge is given by

$$\frac{Q}{Q_0} = \xi_e(1 - \mathrm{e}^{-x/(\xi_e W_d)}) + \xi_h(1 - \mathrm{e}^{(x-W_d)/(\xi_h W_d)}), \tag{68}$$

where W_d is the detector active region width, Q_0 is the initial excited charge magnitude, and x is the event location in the detector, and

$$\xi_{e,h} = \left(\frac{\tau_{e,h} v_{e,h}}{W_d}\right) = \left(\frac{\mu_{e,h} \tau_{e,h} V}{W_d^2}\right), \tag{69}$$

where v is the charge carrier speed, V is the applied operating voltage, and the e and h subscripts denote properties for electrons and holes, respectively. Note that the relative charge collection is dependent upon the interaction location x, and for low values of $\xi_{e,h}$, the energy resolution is poor. Typically, good energy resolution is achieved if $\xi_{e,h} > 50$ for both electrons and holes, where Q/Q_0 has little deviation over the detector width W_d. Otherwise, the energy resolution suffers for higher-energy γ rays ($\gtrsim$300 keV). The value of $\xi_{e,h}$ can be increased by decreasing the detector width W_d, increasing carrier mean free drift times $\tau_{e,h}$ through material improvement, or increasing the applied voltage V. Due to practical voltage limitations and the fundamental difficulty with improving materials, most compound semiconductor detectors are manufactured with small active widths to improve detector energy resolution, and, hence, the devices are relatively small. The $\mu\tau$ values for electrons and holes are often quoted measures of quality for compound semiconductors used as γ-ray spectrometers.

Cryogenic Spectrometers (Microcalorimeters)

Microcalorimeter detectors are energy dispersive spectrometers that measure the thermal change ΔT in an absorber rather than the change in charge concentration ΔQ. The detector consists of an absorber in contact with a type of low-temperature (mK range) thermometer. When absorbed, an x ray produces heat in the absorber material which can then be measured as $\Delta T \approx E/C_h$, where C_h is the heat capacity of the absorber and E is the initial x ray energy. Hence, a measurement of the thermal rise in temperature can yield the photon energy.

Early microcalorimeters used semiconductor thermistors as the thermometer. An x ray absorption causes the resistance in the thermistor to increase, hence producing a change in voltage for current-biased devices. These voltages can be measured as an indication of the ΔT absorbed in the detector. Although effective, yielding energy resolutions below 8 eV for 5.9 keV gamma rays from ^{55}Fe, the resolution is limited by the heat capacity of the absorbers.

The heat capacity is a function of the absorber volume and T^3. In general, the change in FWHM can be approximated by

$$\Delta_{\mathrm{FWHM}} \approx 2.35\eta\sqrt{\mathrm{k}T^2 C_h}, \tag{70}$$

where k is Boltzmann's constant, T is the absolute temperature, and η is an experimental constant dependent upon thermal conductance and heat capacity. From Eq. 70, it becomes clear that the energy resolution improves as the sample volume decreases, yet this resolution improvement comes at the expense of detection efficiency.

Another form of the microcalorimeter utilizes superconducting transition-edge sensor (TES) thermometers. The device is chilled well below the transition edge and heated ohmically by applying a constant voltage bias to the absorber. The bias is adjusted such that the temperature of the device is maintained slightly below the transition edge. The absorption of an x ray causes the superconducting absorber to become normal conducting, thereby increasing the resistance and decreasing the current. The current is measured through induction with a superconducting quantum interference device (SQUID) current amplifier.

Typically the choice of absorber depends greatly upon the photon energy of interest. Energy resolution below 2 eV has been achieved for 5.9 keV gamma rays from ^{55}Fe using Bi absorbers on Mo-Au TES thermometers. Higher-energy gamma rays, yet generally below 100 keV, have good results from superconducting Sn, producing energy resolution below 30 eV for 102 keV gamma rays.

The response time is limited by the heat capacity, in which the reset time is dependent upon the time it takes to return the detector temperature to equilibrium, where the cooling time is represented by $\tau = C_h/G$ where G is the thermal conductance between the thermometer and the cryostat. Arrays of microcalorimeters can be used to maintain fast response time while increasing detection efficiency. Figure 21 shows comparison spectra for a typical HPGe semiconductor detector and a TES microcalorimeter array.

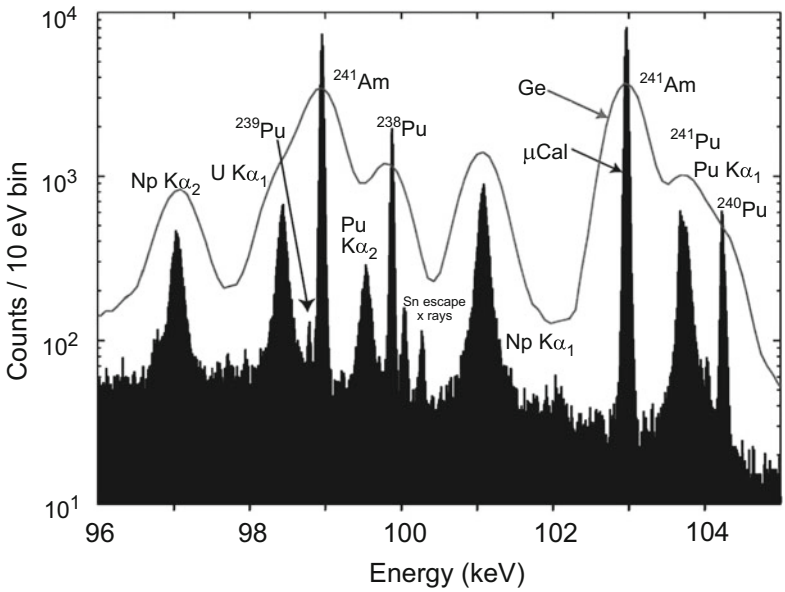

Fig. 21 Pu spectrum from a microcalorimeter array using data from 11 of 13 active pixels. The combined array resolution is approximately 45 eV. At this resolution, the broad x ray peaks can be readily distinguished from gamma-ray peaks. The solid line curve is a spectrum taken with a conventional HPGe detector (c) [2009] IEEE. Reprinted, with permission, from Bacrania et al., *IEEE Trans Nucl Sci*, **56**, 2299–2302, [2009]

Crystal Diffractometers (Wavelength-Dispersive Spectroscopy)

Ultrahigh resolution can be achieved for low-energy gamma rays and x rays with wavelength-dispersive spectroscopy (WDS), which can yield x ray peak resolution better than semiconductor or cryogenic detectors. The method utilizes Bragg scattering, in which the Bragg condition must be satisfied:

$$n\lambda = 2d \sin\theta, \tag{71}$$

where n is an integer, d is the spacing between crystalline planes, λ is the wavelength of the photon under inspection, and θ is the angle at which radiation intersects the crystal from the parallel condition. It is difficult to make a portable system; hence, these instruments are generally attached to an electron microprobe or scanning electron microscope.

Shown in Fig. 22 is a common arrangement for the tool, in which a sample under inspection is irradiated with an electron beam. thereby producing characteristic x rays from the sample. These x rays intersect a slightly bent diffraction crystal. Those x rays satisfying the Bragg condition will diffract into a detector and be recorded, whereas other x rays are absorbed, scatter randomly, or pass through the crystal. Because only the number of counts at a given diffraction angle need be recorded, the detector need not be a high-resolution spectrometer; hence, a gas-filled proportional counter is commonly used as the x ray detector. During operation, the crystal and detector are rotated through a Rowland circle, which allows for the

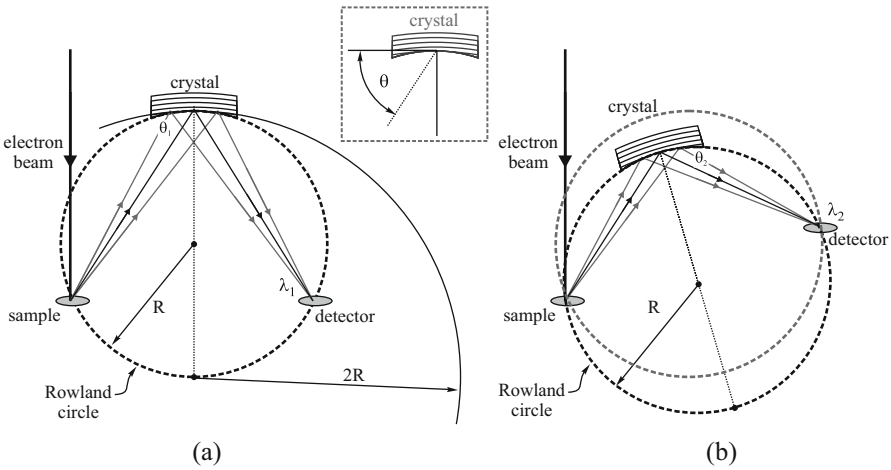

Fig. 22 A typical WDS diffraction arrangement is aligned on a Rowland circle. The sample location remains stationary. The diffraction crystal is bent with a radius twice that of the Rowland circle radius R, and it is typically ground with radius R. The Bragg condition is maintained for various values of λ by moving both the crystal and detector, with the sample remaining stationary, such that all points remain on the Rowland circle

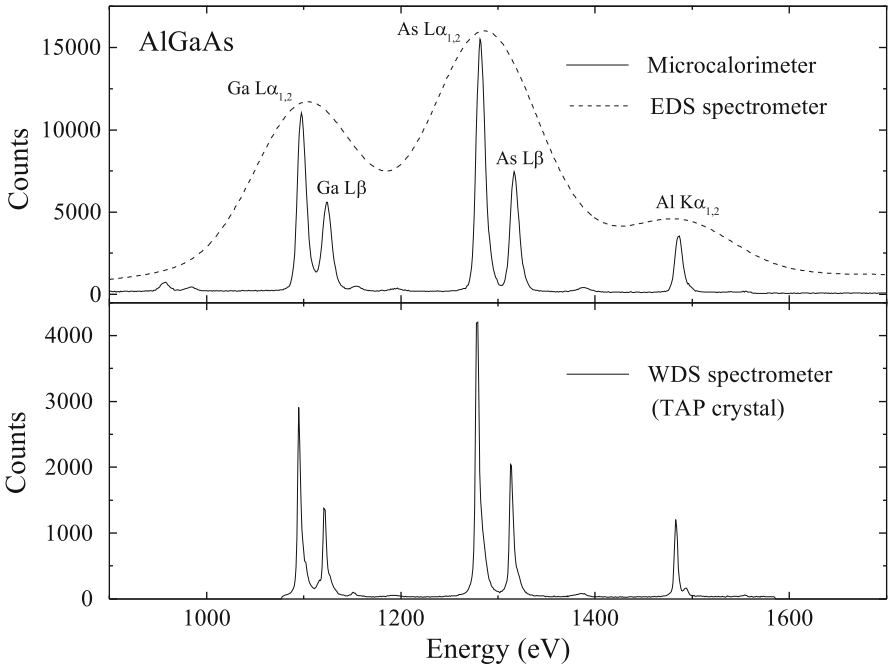

Fig. 23 Shown are (**a**) a comparison of EDS spectra from a Si(Li) detector and a microcalorimeter detector and (**b**) an additional comparison to a WDS detector. Reproduced from Wollman et al., *J Microscopy*, **188**, 196–223, (1997) with the permission of Wiley Publishing

Bragg condition to be maintained as the arrangement rotates through a continuum of wavelengths.

As a result, the x ray detector records the number of counts as a function of wavelength. The stringent requirement for the Bragg condition results in ultrahigh resolution, which can be plotted as a function of photon energy (see Fig. 23). The important advantage of WDS is the superior identification ability it provides to the user. Unfortunately, the system can be used only on photons of energy low enough to Bragg diffract. Several commercial systems have a rotating rack of different diffraction crystals that extend the sensitive range. WDS systems are laboratory-based and hence are not generally considered portable.

Summary

Gamma-ray spectroscopy seeks to determine, first, the gamma-ray energies emitted by a sample or the nuclides (which emit gamma rays of certain energies) present within a sample. This goal can be called *qualitative analysis*. However, generally, one also seeks either the source strength of the particular gamma rays or the concentration of the nuclide emitting the gamma rays. This desired outcome is often referred to as *quantitative analysis*.

One achieves the objectives of gamma-ray spectroscopy by analyzing spectra. In this chapter, pulse-height spectra in which number of counts are specified by discrete channel number are considered. This approach is used because channel number is directly proportional to pulse height and photon energy can then be obtained from pulse height whether or not the spectrometer is linear. Spectroscopic analysis techniques begin by attempting to determine the continuous channel number that corresponds to the centroids of the full-energy peaks in the spectrum that are of interest. The MCLLS approach focuses on the entire spectrum and seeks to determine the parameters of models that best fit all or major portions of the spectra. The symbolic Monte Carlo approach holds promise for spectroscopic applications in which the model is nonlinear in terms of the nuclide concentrations of samples.

Depending upon the need, there are several devices that can be used for gamma-ray spectroscopy. Efficiency with adequate energy resolution can be provided with large volume scintillators, whereas high-energy resolution can be achieved with semiconductor detectors. Both scintillator and semiconductor detectors can be acquired as portable units with good detection efficiency for gamma rays. For ultrahigh-energy resolution, microcalorimeters or WDS diffractometers offer excellent performance. Yet, microcalorimeters and WDS spectrometers are generally restricted to laboratory-based instrumentation for low-energy gamma rays and x rays. Note that the spectrometers discussed in the present chapter represent only a select sample of variations commercially available. More information can be found in the book chapters dedicated to semiconductor and scintillation detectors.

Cross-References

▶ Scintillators and Scintillation Detectors
▶ Semiconductor Radiation Detectors

References

Bacrania MK et al (2009) Large-area microcalorimeter detectors for ultra-high-resolution x ray and gamma-ray spectroscopy. IEEE Trans Nuc Sci 56(4):2299–2302

Barache D, Antoine J-P, Dereppe J-M (1997) The continuous wavelet transform, an analysis tool for NMR spectroscopy. J Magn Res 128:1–11

Bevington PR (1969) Data reduction and error analysis for the physical sciences. McGraw-Hill, New York

Cline JE (1968) Studies of detection efficiencies and operating characteristics of Ge(Li) detectors. IEEE Trans Nucl Sci NS-15:198–213

Dunn WL (1981) Inverse Monte Carlo analysis. J Comput Phys 41(11):154–166

Dunn WL, Dunn TS (1982) An assymetric model for XPS analysis. Surf Interface Anal 4(3):77–88

Dunn WL, Shultis JK (2009) Monte Carlo analysis for design and analysis of radiation detectors. Radiat Phys Chem 78:852–858

Gardner RP, Sood A (2004) A Monte Carlo simulation approach for generating NaI detector response functions (DRF's) that accounts for nonlinearity and variable flat continua. Nucl Instrum Methods B213:87–99

Gardner RP, Xu L (2009) Status of the monte carlo library least-squares (MCLLS) approach for non-linear radiation analyzer problems. Radiat Phys Chem 78:843–851
Gentile NA (2001) Implicit monte carlo diffusion – an acceleration method for monte carlo time-dependent radiative transfer simulations. J Comput Phys 172:543–571
Gilmore G (2008) Practical gamma-ray spectrometry, 2nd edn. Wiley, New York
Haitz RH (1961) Model of the electrical behavior of a microplasma. J Appl Phys 35:1370–1376
Heath RL, Helmer RG, Schmittroth LA, Cazier GA (1967) Method for generating single gamma-ray shapes for analysis of spectra. Nucl Instrum Methods 47:281–304
IEEE/ANSI (1996) IEEE standard test procedures for germanium gamma-ray detectors, standard 325–1996
Kargar A, Brooks AC, Harrison MJ, Chen H, Awadalla S, Bindley G, McGregor DS (2009) Effect of crystal length on CdZnTe frisch collar device performance. In: IEEE Nucl Sci Symp Conf Rec, Orlando, 24 Oct–1 Nov, pp 2017–2022
Kis Z, Fazekas B, Östör J, Révay Z, Belgya T, Molnár GL, Koltay L (1998) Comparison of efficiency functions for Ge gamma-ray detectors in a wide energy range. Nucl Instrum Methods A418:374–386
Marshall III JH, Zumberge JF (1989) On-line measurements of bulk coal using prompt gamma neutron activation analysis. Nucl Geophys 3:445–459
McGregor DS (2016) Detection and measurement of radiation, Ch 8. In: Shultis JK, Faw RE (eds) Fundamentals of nuclear science and engineering, 3rd edn. CRC Press, New York
McGregor DS (2018) Materials for gamma-ray spectrometers: inorganic scintillators. Ann Rev Mater Res 48:13.1–13.33
McGregor DS, Shultis JK (2020) Radiation detection: concepts, methods, and devices. CRC Press, Boca Raton
McIntyre RJ (1961) Theory of microplasma instability of silicon. J Appl Phys 32:983–995
Mickael MW (1991) A complete inverse Monte Carlo model for energy-dispersive x ray fluorescence analysis. Nucl Instrum Methods A301:523–542
Molnar GL (2004) Handbook of prompt gamma activation analysis with neutron beams. Kluwer Academic Publishers, Boston
Moré JJ, Garbow BS, Hillstrom KE (1980) User's guide for MINPACK-1, Report ANL-80-74, Argonne National Laboratory
Nafee SS (2011) A mathematical approach to determine escape peak efficiencies of high-purity germanium cylindrical detectors for prompt gamma neutron activation analysis. Nucl Tech 175:162–167
Press WH, Teukolsky SA, Vetterling WT, Flannery BP (1992) Numerical recipes in FORTRAN 77. The art of scientific computing, 2nd edn. Cambridge University Press, New York
Renker D (2006) Geiger-mode avalanche photodiodes, history, properties and problems. Nucl Instrum Methods A567:48–56
Wollman DA, Irwin KD, Hilton GC, Dulcie LL, Newbury DE, Martinis JM (1997) High-resolution, energy-dispersive microcalorimeter spectrometer for x ray microanalysis. J Microscopy 188(3):196–223
Xu Y, Weaver JB, Healy DM Jr, Lu J (1994) Wavelet transform domain filters: a spatially selective noise filtration technique. IEEE Trans Image Proc 3(6):747–758
Yacout AM, Dunn WL (1987) Application of the inverse monte carlo method to energy-dispersive x ray fluorescence. Adv x ray Anal 30:113–120

Further Reading

Birks JB (1964) The theory and practice of scintillation counting. Pergamon Press, Oxford
Enss C (ed) (2005) Cryogenic particle detectors, vol 99, In: Topics in applied physics. Springer, New York

Goldstein JI, Newbury DE, Echlin P, Joy DC, Fiori C, Lifshin E (1981) Scanning electron microscopy and x ray microanalysis. Plenum Press, New York
Hornbeck RW (1975) Numerical methods with numerous examples and solved illustrative problems. Quantum Publishers, New York
Knoll GF (2010) Radiation detection and measurement, 4th edn. Wiley, New York
Owens A (2019) Semiconductor radiation detectors. CRC Press, Boca Raton
Price WJ (1964) Nuclear radiation detection, 2nd edn. McGraw-Hill, New York
Rodnyi PA (1997) Physical processes in inorganic scintillators. CRC Press, Boca Raton
Schlesinger TE, James RB (1995) Semiconductors for room temperature nuclear detector applications. In: Semiconductors and semimetals, vol 43. Academic Press, San Diego
Tsoulfanidis N, Landsberger S (2015) Measurement and detection of radiation, 4th edn. CRC Press, Boca Raton

Radiation Spectrometer Suppliers

- AmpTek-Ametek; www.amptek.com
- Baltic Scientific Instruments; bsi.lv/en/
- Berkeley Nucleonics Corp.; www.berkeleynucleonics.com
- Dynasil; www.dynasil.com
- Eurorad; www.eurorad.com/detectors.php
- Itech Instruments; www.itech-instruments.com/
- Kromek; www.kromek.com/
- Ludlum Measurements, Inc.; `ludlums.com`
- Mirion Technologies; www.canberra.com/cbns/
- Moxtek; www.moxtek.com/
- Ortec-Ametek; www.ortec-online.com/
- Radiation Monitoring Devices `dynasil.com/rmd`
- Redlen Technologies; www.redlen.com/
- Saint Gobain; www.crystals.saint-gobain.com/
- Scionix; `scionix.nl`